Interaction of Silver Nanoparticles with a Lipid Bilayer Membrane and a Polymer Mesh

by

Prashant Mishra

A dissertation submitted for the partial fulfilment of

BS-MS dual degree in Science

INDIAN INSTITUTE OF SCIENCE EDUCATION AND RESEARCH, MOHALI

May 2012

Declaration of Authorship

The work presented in this dissertation has been carried out by me under the guidance of **Dr. Kavita Dorai** at Indian Institute of Science Education and Research Mohali.

This work has not been submitted in part or in full for a degree, a diploma, or a fellowship to any other university or institute. Whenever contributions of others are involved, every effort is made to indicate this clearly, with due acknowledgment of collaborative research and discussions. This thesis is a bonafide record of original work done by me and all sources listed within have been detailed in the bibliography.

Signed:

Date:

In my capacity as the supervisor of the candidate's project work, I certify that the above statements by the candidate are true to the best of my knowledge.

Signed:

Date:

Certificate of Examination

This is to certify that the dissertation titled "**Interaction of Silver Nanoparticles with a Lipid Membrane and a Polymer Mesh.**" submitted by **Mr. Prashant Mishra** (Reg. No. MS07017) for the partial fulfilment of BS-MS dual degree programme of the institute, has been examined by the thesis committee duly appointed by the Institute. The committee finds the work done by the candidate satisfactory and recommends that the report be accepted.

Dr. Rajeev Kapri	Dr. Ananth Venkatesan	Dr. Kavita Dorai (Supervisor)
Date:	Date:	Date:

Abstract

Nanoparticles are the new technological revolution in the field of medicine. Different kind of nanoparticles are being used for different purposes. Targeted drug delivery is the main aim to fulfill through the use of these nanoparticles. The physical properties of these nanoparticles vary with reference to the feature of the target. Magnetic Nanoparticles(Fe_2O_3), Gold Nanoparticles(AuNP), Silica Nanoparticles(SiO_2), Silver Nanoparticles(AgNP) are some examples which have been regularly used in medicinal purposes. Now since the delivery of drug to the target is through a path which contains different parts of cell so studying the interaction with those parts is also part of the problem as that affect the effciency of targeted delivery. Lipid bilayer membrane is a part of a cell through which our nanoparticle makes it's way to the target. There are various studies[1–3] of the interaction between lipid membrane and nanoparticle. Here we have studied the phase behavior of the lipid membrane with and without nanoparticle at a temperature range from 10°C to 40°C through ^{31}P Nuclear Magnetic Resonance(NMR). We have compared T_1 Relaxation time, T_2 Relaxation time, Diffusion Coefficient, Hydrodynamic Radius of the same. A significant difference have been found in these values at various temperature and also phase transition temperature has shown some shift in the values.

Interaction studies of Nanoparticle and Polymer Mesh is also important as polymer meshes work as a vesicle for these nanoparticle to reach the target. Various studies suggested that Triblock Copolymer have a property to form better mesh than other normal polymer which is why it has been used in this area for a long time as a vesicle for nanoparticle. We studied the effect of nanoparticle on the correlation in between the bond of Triblock Copolymer through 1D Proton NMR & 2D COSY NMR. A significant shift has been found at some peaks which shows strong interaction of nanoparticle and Triblock Copolymer.

Acknowledgements

I would like to acknowledge the guidance and encouragement of my supervisor, Dr. Kavita Dorai. Her expertise in this field have been priceless to me throughout my project work.

I would like to thank Mrs. Amrita Kumari, Ms. Shruti, & Ms. Navdeep Gogna wholeheartedly for the many helpful discussions, advice, experiments, suggestions, and at the same time keeping the lab environment so healthy and productive. I heartfully thank my lab members M.N. Shukla, Rajesh, Ritabarata & Debmalya for providing wellwishes during the stress moments like presentations.

Furthermore, I thank our Director Prof. N. Sathyamurthy for giving me such a nice opportunity and institutional funding for my project work. I truly appreciate staff's efforts to accommodate all of my research needs as soon as possible. In addition to professional support, I cannot overemphasize the value of the support and encouragement I have received from the many friends I have made in IISER Mohali over the last five years. While there are too many people to list here, at the very least I must offer my most heartfelt thanks to Rajni Ranjan, Parul Gupta, Amita Agarwal, Amol Deshmush, Amol Ratnaparkhe who dragged me out of the lab when I needed it the most, listened to my complain, helped me keep things in perspective, but most importantly, provided me with endless laughs and entertainment, and the breaks I needed in order to stay focused. I would also like to thank our canteen caterer Vishvajeet who provided snacks and tea whenever I was with my friends during the breaks.

Contents

List of Figures

List of Tables

Abbreviations

AgNP	**S**ilver **N**anoparticles
PEG	**P**oly **E**thylene **G**lycol
PPG	**P**oly **P**ropylene **G**lycol
NMR	**N**uclear **M**agnetic **R**esonance
^{31}P	**31 P**hosphorous
^{1}H	**1 H**ydrogen
^{13}C	**13 C**arbon
^{15}N	**15 N**itrogen
M	**M**agnetization
N	**N**umber of spins
1D	**1 D**imensional
2D	**2 D**imensional
DOSY	**D**iffusion **O**rdered **S**pectroscop**Y**
COSY	**CO**rrelations **S**pectroscop**Y**
NOESY	**N**uclear **O**verhauser **E**ffect **S**pectroscop**Y**
TOCSY	**TO**tal **C**orrelation **S**pectroscop**Y**
S/N	**Signal** to **Noise** Ratio
PGSE	**P**ulsed **F**eld **G**radient **S**pin **E**cho
DPPC	**D**i **P**almitoyl **P**hosphatidyl **C**holine
FID	**F**ree **I**nduction **D**ecay

Symbols

I	Spin Quantum Number
B	Magnetic Field
$\mathbf{B}$	Magnetic Field Vector
B_0	Static Magnetic Field
B_1, $B_{r.f.}$	Radio-Frequency Field
ΔB_0	offset field
B_{eff}	Effective Field
F	Fourier Transform
H(ω)	Frequency Response Function
h(t)	Impulse Response Function
μ	Nuclear Magnetic Moment
ω	Angular Frequency
γ	Gyromagnetic Ratio
θ	Tilt Angle
T_1	Longitudinal Relaxation
T_2	Transverse Relaxation
ν	Linear Frequency
α	Spin State $\|M = +1/2\rangle$
β	Spin State $\|M = -1/2\rangle$
τ	Relaxation time
η	Viscosity

k	Boltzmann Constant
r_s	Radius of Solute
T	Temperature
D	Diffusion Coefficient

Chapter 1

Introduction

1.1 NMR Signal

The phenomenon of Nuclear Magnetic Resonance(NMR) depends on the magnetic properties of atomic nuclei. Atomic nuclei can be of three types:

- (a) Nuclei with odd number of total Nucleons(Proton + Neutron)
- (b) Nuclei with even number of Neutrons and even number of Protons
- (c) Nuclei with odd number of Neutrons and odd number of Protons

Nuclei with an odd number of Nucleons will have a half-integral spin quantum number as only one nuclear spin will be unpaired. On the other hand nuclei with even number of nucleons will have either zero spin quantum number as neutron and proton each get paired or are integral spin quantum number where one unpaired neutron and one unpaired proton contribute to the spin quantum number.

Since the NMR phenomenon depends only on the existence of nuclear spin thus nuclei of category (b) are NMR inactive. Most common NMR nuclei include ^{1}H,^{13}C,^{15}N and ^{31}P (spin 1/2) and $^{2}H_1$ (spin 1).

The energy diagram for two spin states of nuclei with $I = \frac{1}{2}$ has its classical equivalent in the parallel(ground state) and antiparellel(excited states) orientation of z-component of nuclear magnetic moment μ relative to the external field B_0. In this model, absorption of energy via interaction of the electromagnetic radiation with the nuclear moment leads to inversion of the magnetic vector μ. [4]

The magnetic dipole in a homogeneous magnetic field B_0 experiences a torsional moment that attempts to align it with the direction of the field. The angular momentum of the nucleus therefore causes a precessional motion of μ around the z-axis that can be easily understood according to the principles of gyration. The angular velocity of this precessional motion, known as Larmor precession, is given by $\omega_0 = -\gamma B_0$, since the vector ω_0 points the negative z-direction. The **Larmor frequency** is thus

$$\omega_0 = \gamma B_0 \tag{1.1}$$

For the resonance process it is important to note that a magnetic field B_1(r.f. Pulse) can effect the inversion of the magnetic moment μ mentioned above. In order to achieve this, B_1 must be directed at right angles to x, y-component of μ and rotate in the x,y-plane with an angular velocity equal in sign and magnitude to the Larmor frequency. At this point it proves advantageous to introduce, in addition to the fixed coordinate system $C(x, y, z)$, known as *laboratory frame*, a rotating coordinate system $C'(x', y', z')$. In this *rotating frame*, the magnetic moment no longer feels the effect of the static magnetic field B_0 but rather that of a magnetic field

$$B' = B_0 + \omega/\gamma \tag{1.2}$$

where ω is the angular velocity of C' and ω/γ is a fictitious field B_f that exists only as a result of the relative motion of the coordinate systems C and C'. For $\omega = 0$, B_f vanishes while for $\omega = -\gamma B_0$, B' becomes zero. This obviously corresponds to the statement that the vector assumes a fixed position in the rotating frame if ω is equal

both in sign and magnitude to the Larmor frequency. The angular velocity and sign of rotation of C' then coincides with the precessional motion.

If we now turn on the magnetic field B_1 that is assumed stationary in the rotating frame and directed along the x'-axis perpendicular to B_0, the effective field according to Equation 1.2 is given by

$$B_{eff} \begin{cases} = B' + B_1 \\ = B_0 + \omega/\gamma + B_1 \\ = B_0(1 - \omega/\omega_0) + B_1 \end{cases} \tag{1.3}$$

The angle θ formed by B_{eff} with the z-axis is defined by

$$\tan\theta = \frac{B_1}{B_0(1 - \frac{\omega}{\omega_0})} \tag{1.4}$$

With the condition $B_0 \gg B_1$ for the magnitude of the individual fields variation of B_0 and thus Larmor frequency ω_0 (Equation 1.1) leads to the following situation:

1. If the magnitude of ω_0 and β are very different, the effective field is aligned *parallel* to the z-axis, because according to Equation 1.4, $\tan\theta$ becomes approximately equal to zero, i.e. $\theta \approx 0°$or $180°$for $\omega_0 < \omega$ or $\omega_0 > \omega$, respectively$(B_0 \gg B_1)$.

2. On the other hand, if $\omega_0 \approx \omega, \tan\theta$ approaches ∞ and $\theta = 90°$; B_e is then equal to B_1 and the vector μ precesses with frequency ω_1 around the direction of B_1, that is around the x'-axis. Thus, μ passes from the ground to the excited state. Because $B_0 \gg B_1$ this situation represents a typical resonance phenomenon, since a small periodic perturbation of the system leads to a large variation. The system is affected by the perturbing field, however, only when the Larmor frequency and the frequency ω are identical.

In practice, the rotating field B_1 is generated by an oscillator along the x-axis of the fixed coordinate system C. A magnetic field B_x linearly polarized in the x-direction

with frequency ω and the amplitude $2B_1$ can be represented by two rotating magnetic vectors $B_1(l)$ and $B_1(r)$, one of which, $B_1(r)$, has the desired rotational sense. The other vector has practically no effect on the experiment. The foregoing model was based upon an isolated nucleus. We now extend our analysis to a macroscopic sample and thus to a large number of nuclei.

After turning on the magnetic field B_0, the nuclei approach an equilibrium distribution between energy levels α and β. This process, which occurs within a certain time interval, yields $N_\beta > N_\alpha$ according to the Boltzmann distribution law. The result of this process is the build-up of macroscopic equilibrium magnetization M of the magnitude M_0, which is the resultant of individual magnetic moments of those nuclei that form the excess population of the ground state. Since the nuclear moments do not rotate in phase but are statistically distributed over a conical envelope, no component of the macroscopic magnetization in the x,y plane exists. By means of a transmitter on the x-axis, a linearly polarized electromagnetic field B_1 of the frequency ω and amplitude $2B_1$ stationary in the rotating frame is now generated. At resonance($\omega_0 = \omega$) an interaction between the individual nuclear moments and the field B_1 occurs, which deflects **M** from its equilibrium position along the z-axis. This is turn creates a finite transverse magnetization $M_{y'}$ in the y'-direction. In contrast to the case for individual nuclear magnetic moments, here the vector **M** is not inverted, because when the amplitude of B_1 is small, not all nuclear moments μ can absorb energy. Consequently, in the fixed coordinate system, **M** executes a precessional motion around the z-axis. [4]

As a result the transverse magnetization produced also rotates in the coordinate system C and can be detected by means of a receiver coil along the y-axis. The deviation of **M** is proportional to the energy take-up of the spin system from the r.f. field B_1 and the Continuous Wave(CW) N.M.R. signal corresponds to the stationary state between nuclear excitation and relaxation.

Since the ideal case, in which all nuclei of a macroscopic sample have the same Larmor frequency, is not encountered in practice, a transverse magnetization is induced both before and after attainment of the exact resonance condition. When ω_0 is varied sufficiently slowly, the vector $\mathbf{M}$ traces a circle in the rotating frame. If one plots its components $M_{x'}$ and an absorption curve for $M_{y'}$(symbolized by u and v, respectively) as a function of the frequency difference $\Delta\omega = \omega_0 - \omega$, one obtains a dispersion curve for $M_{x'}$ and an absorption curve for $M_{y'}$. The components of the transverse magnetization differ in phase by 90°, but both can be measured, since according to Faraday's law the induced electric current in the fixed coordinate system C is proportional to the periodic variation dM_x/dt or dM_y/dt.

The quantitative mathematical basis for the phenomenological treatment (Appendix D) was developed by Bloch. It culminates in the famous *Bloch equations*. The transverse magnetization $M_{y'}$ which corresponds to the absorption signal is given by:

$$M_{y'} = \frac{-M_0\gamma B_1 T_2}{1 + T_2^2(\omega_0 - \omega)^2 + \gamma^2 B_1^2 T_1 T_2} \tag{1.5}$$

Similar relationships are obtained for $M_{x'}$ and, correspondingly, for M_y and M_x in the laboratory frame.

1.2 Relaxation

Two macroscopic magnetizations are distinguished in an NMR experiment: the longitudinal magnetization along the z-axis and the transverse magnetization in the x,y plane. Both are subject to relaxation phenomena, i.e., their magnitudes are time-dependent.

1.2.1 Longitudinal Relaxation Time (T_1)

Immediately after exposing the spins of a sample to the external magnetic field B_0, they are in a non-equilibrium state because all spin states are equally populated and $M_0 = 0$. The build-up of the equilibrium magnetization M_0 then requires a time T_1 and the variation of the z component of the macroscopic magnetization obeys a first-order differential equation:[4]

$$dM_z/dt = (M_0 - M_z)/T_1 \tag{1.6}$$

$1/T_1$ is thus the rate constant for the transition of the perturbed system to the equilibrium state. During T_1, energy is transferred from the spin to environment, the so called *lattice*. This process, is called *longitudinal relaxation*. Accordingly, T_1 is known as the *longitudinal* or *spin-lattice relaxation time*.

relaxation plays an important role in the observation of the resonance phenomenon. The magnitude of the new equilibrium magnetization M_z is a function of the longitudinal relaxation time and the amplitude of the B_1 field. As can be derived for B_1 fields, the maximum intensity I of the CW signal at $\omega = \omega_0$ is given by

$$I(\omega_0) = constant/B_1T_1 \tag{1.7}$$

Long relaxation times T_1 and the high amplitude of the oscillating field therefore reduce the signal intensity, i.e. saturate the resonance line. [4]

Shorter relaxation times, on the other hand, broaden the resonance lines. This arises because the lifetime of nuclei in the exited state is decreased, which causes an uncertainty in the determination of the energy difference. According to the uncertainty principle $\Delta E \Delta t \approx h$ and with $\Delta E = h\Delta\nu$ this leads to $\Delta\nu\Delta t \approx 1/2\pi$ or $\Delta\nu = 1/2\pi\Delta t$ for the uncertainty in the determination of the resonance frequency. The line width

therefore contains the quantity $1/\Delta t$ or $1/T_1$. in organic liquids T_1 for protons is generally in the order of a few seconds or less so that spin-lattice relaxation contributes not more than 0.1 Hz to the line width.

Now, by which mechanism is energy exchanged between the lattice and the nuclear spin system? In liquids magnetic dipole-dipole interaction is mainly responsible and thus is significant for high-resolution NMR even if it does not lead to a line splitting. Rotational and translational motions of a molecule in a liquid occasion a fluctuation, i.e. time-dependent magnetic field, which can be described simply as magnetic noise. This fluctuating field possesses components $B_{x'}$ and $B_{y'}$ with frequency ω_0 which satisfies the resonance condition and can stimulate transitions. The magnetic energy received by the lattice is then transformed into thermal energy. The longitudinal relaxation process is especially effective if paramagnetic substances are present in the solution. This is because the relaxation time T_1 theoretically is inversely proportional to the square of the magnetic moment that gives rise to the above mentioned fluctuating field. The magnetic moment of an unpaired electron is larger than the nuclear magnetic moment by a factor of about 10^3. T_1 therefore become smaller than 10^{-1} s and the resonance lines become very much broadened. [4]

1.2.2 Transverse Relaxation(T_2)

In the classical description of the NMR experiment, in addition to the z-magnetization there exists a second magnetization in the x,y plane, usually termed transverse magnetization($M_{x,y}$). It seems therefore reasonable to introduce a second relaxation time T_2, the so-called transverse relaxation time, especially since it turns out that the time dependence of $M_{x,y}$ usually differs from that observed for M_z. T_2 is also known as the spin-spin relaxation time after the mechanism responsible for transverse relaxation(energy transfer between individual spins).

Another justification for the introduction of T_2 comes from the consideration of the line width of the NMR transitions. As was mentioned above, longitudinal relaxation usually contributes less than 0.1 Hz. Nevertheless, observed line widths are larger and may amount to several kilohertz in the case of solids. It is therefore convenient to define another characteristic time T_2 , shorter than T_1, to deal with this situation.

In the simplest case $T_2 = T_1$ for liquids since, after resonance, the x,y-component of the magnetization vanishes at the same rate as the longitudinal magnetization attains its previous value M_0 along the z-axis. On the other hand, the transverse magnetization can be reduced without the simultaneous increase in the z-component($T_2 < T_1$). As in the case of spin-lattice relaxation, fluctuating field can interact with the transverse component $M_{x,y}$, thereby reducing its magnitude. Whereas time dependent fields $B_{x'}(t)$ and $B_{y'}(t)$, stationary in the rotating field, interact with M_z, $M_{x,y}$ can interact not only with $B_{x'}(t)$ and $B_{y'}(t)$ but also with B_z. The component B_z, however, is static in the laboratory frame; thus transverse relaxation can also originate from the presence of static dipolar fields.

An important mechanism for transverse relaxation is based on an energy transfer with the spin system. Any transition of a nucleus between its spin states changes the local field at nearby nuclei at the correct frequency to stimulate a transition in the opposition direction. The lifetime of the spin states will be shortened by this process and it therefore contributes to the NMR line width in a manner similar to the spin-lattice relaxation process. The total energy of the spin system does not change, however, and transverse relaxation of this kind can be regarded as an entropy process. Spin-lattice relaxation, on the other hand, is classified as an enthalpy process.[4]

In liquids, the inhomogeneity, ΔB_0, of the magnetic field B_0 is by far the most important factor for the time dependence of $M_{x,y}$. Exposure of the individual nuclear spins to different external fields $B_0 \pm \Delta B_0$ will result in a spread of their Larmor frequencies and in a fanning out process for $M_{x,y}$. In order to avoid the resulting line broadening,

each determination of an NMR spectrum should be preceded by optimization of field homogeneity through adjustment of the field gradients.

According to the quantitative classical treatment of the resonance process, for small amplitudes of the B_1 field, i.e. for $\gamma^2 B_1^2 T_1 T_2 \ll 1$, the resonance signal is described by

$$I(\omega) = \frac{constant \times B_1 T_2}{1 + (\omega_0 - \omega)^2 T_2^2} \tag{1.8}$$

The signal intensity at the point of resonance ($\omega = \omega_0$) is then proportional to the transverse relaxation signal:

$$I(\omega_0) = constant \times B_1 T_2 \tag{1.9}$$

Including B_1 in the constant, it follows for the intensity at half the signal height that

$$I_{1/2} = constant \times \frac{1}{2} T_2 \tag{1.10}$$

As this value for $I_{1/2}$ must also satisfy equation for $I(\omega)$, there results

$$\frac{T_2}{2} = \frac{T_2}{1 + (\omega_0 - \omega)^2 T_2^2} \tag{1.11}$$

and one obtains

$$\omega_0 - \omega_{1/2} = \frac{1}{T_2} \text{or} \Delta = \frac{2}{T_2} \tag{1.12}$$

where Δ is the line width of resonance signal at half-height. Since the decay of $M_{x,y}$ is caused by field inhomogeneity and natural spin-spin relaxation as well, one usually writes

$$\Delta = \frac{2}{T_{2\star}} \tag{1.13}$$

with

$$\frac{1}{T_{2\star}} = \frac{\gamma \Delta B_0}{2} + \frac{1}{T_2} \tag{1.14}$$

where the first term is the inhomogeneity contribution to the line width. In hertz one

has $\Delta = 1/\pi T_2\star$ if $T_2\star$ is measured in seconds. Equation of $I(\omega)$ describes a *Lorentz curve* and the signal is said to have a *Lorentzian line shape.*[4]

1.3 2D NMR

No other development has influenced magnetic resonance spectroscopy in the last twenty years so profoundly as the concept of two-dimensional(2D) NMR. This technique, which emerged from an idea of the Belgian physicist Jeener, has been developed for applications primarily in the laboratories of R.R. Ernst at the ETH Zurich and R. Freeman at the University of Oxford. Today it forms the basis for a large number of experiments in all branches of NMR. [4]

The 2D NMR experiment is basically characterized by three intervals: *preparation*, *evolution* and *detection*. In a number of 2D experiments a further interval is added before detection, the so-called *mixing time*.

During the preparation time the spin system of the interest is prepared for the experiment, for example by application of decoupler experiments or simply by the generation of transverse magnetization through a 90°pulse. In the evolution time t_1 it then develops under the influence of different factors, as for example Larmor precession or scalar spin-spin coupling, before a signal is detected during the detection time t_2.[4]

Only if in a series of experiments the sequence is repeated with a systematic variation of the evolution time t_1 by adding time increments Δt_1, and if after the first Fourier transformation of the resulting t_2 signals a number of one-dimensional spectra is obtained in the frequency domain F_2 which shows a modulation in amplitude or phase, can a second Fourier transformation be applied. The data of these spectra are then transformed with respect to the time axis t_1. A frequency axis F_1 results which now contains the frequencies of those mechanisms which have been effective during the evolution time t_1 and which caused the observed modulation of signal amplitude or

signal phase. If for instance spin-spin coupling was effective during t_1 and Larmor precession during t_2, F_1 contains coupling constants while the chemical shifts appear on the frequency axis F_2. Resonance frequencies and spin-spin coupling constants which are a priory indistinguishable in a conventional one-dimensional NMR spectrum can thus be separated and presented on two distinct frequency axes.[4]

A 2D NMR experiment is possible only after a series of n 1D spectra has been measured. Thereby the evolution time is systematically increased by adding time increments Δt_1: Normally 32 1D experiments are used as a minimum, but 128 or 256 single 1D experiments are not uncommon.

The experimental data of such a series of 1D experiments are not individually Fourier-transformed but rather stored in the computer memory. They yield a data matrix which is characterized by two time axes: t_1 and t_2. The 2D spectrum is thus a function of two variables: $\mathrm{S}(t_1, t_2)$. A first Fourier transformation with respect to t_2 yields $\mathrm{S}(t_1, F_2)$. This function must be seen as a series of one dimensional spectra, the signals of which are modulated with respect to their amplitude or phase. There exists a periodical behavior along t_1. The final 2D spectrum is thus a function of two frequencies variable: $\mathrm{S}(F_1, F_2)$.

Only the detection time is a real time axis in 2D experiment, that is, real FID signals are only detected in t_2. In contrast, the FID for Fourier transformation along t_1 is constructed point by point. Therefore, the t_1 increments Δt_1 determine the Nyquist frequency in the F_1 domain. Thus a value of 1 ms for Δt_1 means, for example, that along t_1 frequencies of 1 kHz can be recognized if quadrature detection can be used in t_1. The t_1 increment Δt_1 thus corresponds to the dwell time of the t_1 dimension. Quadrature detection in t_1 can be achieved through certain phase cycles, which yields a phase shift of 90°for the receiver signal. Two experiments must then be performed for each t_1 increment.

Normally long measuring times are required for 2D NMR. This is also due to the fact that nearly always 90°excitation pulses are used. Therefore. after each individual

t_1 experiment a relaxation delay is necessary in order to provide uniform starting conditions. Finally the mass of data which has to be mathematically processed is much larger than in 1D experiment. Without modern computers, especially efficient data storage capacities, 2D NMR would not be practicable.[4]

1.4 Pulsed Field Gradients

The pulsed field-gradient spin-echo(PGSE) NMR method dates back to the year 1965. In the 46 years that have elapsed since this pioneering work, a large number of publications have dealt with the study of molecular-self-diffusion in systems of various complexity.[5] In the most basic form, the PGSE experiment is based on the 90°-τ-180°spin-echo radio frequency sequence used in, the Carr-Purcell method for spin-spin(T_2) relaxation measurements to which magnetic-field gradients have been added. At a time τ after the 180°pulse a spin-echo is formed. If the Fourier transformation starts at this point, the resulting spectrum will be essentially identical to the one obtained using an ordinary 90°RF pulse sequence, except for the attenuation of the various signals, brought about by the spin-spin relaxation over the time span of 2τ. This attenuation is in principle given by $\exp(-2\tau/T_2)$. The value of T_2 are different from one component to the other, and also in principle from one NMR signal to another in the same component. Therefore, there will always be a restriction on the range of τ that may be used in such experiments.[5] There are two main ways in which NMR may be used to study self-diffusion coefficients, which are also known as tracer-diffusion or intradiffusion coefficients (a)analysis of relaxation data and (b) pulsed-field gradient (PFG) NMR. However, the two methods report on motions in very different time scales and thus, even though a translational diffusion coefficient can be derived in both cases, the two estimates will agree only under certain circumstances. since the relaxation method is in fact sensitive to rotational diffusion, whereas the PFG method measures translational diffusion. Generally, in experiments involving the solution state, relaxation measurements are sensitive to motions occurring in the

picosecond to nanosecond time scale-that is, motion on the time scale of the reorientational correlation of the nucleus. While in PFG measurements, motion is measured over the millisecond to second time scale.[5] In the first method, relaxation data are analyzed to determine the rotational correlation time(s) (τ_c) of a probe species.τ_c can then be related to the solution viscosity, and ultimately, to the translational diffusion coefficient by using the Debye equation

$$\tau_c = 4\pi\eta r_s^3/(3kT) \tag{1.15}$$

and the Stokes-Einstein equation, However, a number of assumptions which, depending upon the system being studied, may or may not be justified need to be made in performing this analysis. First, the relaxation mechanism of the probe species needs to be known, and it is required that the intermolecular contributions to the relaxation can be separated from the intramolecular contributions. Second, only if the molecule is spherical can its rotational dynamics be properly characterized by a single correlation time. Third, depending on the size of the probe molecules compared to the molecules of the bulk solution, they may not see the solution as being continuous; as a consequence, one of the basic requirements for the validity of the Debye equation is violated. Thus, serious assumptions are involved in applying this method to studying biological systems when a small probe species is used since the solution normally has a large macromolecular component (e.g., a large part of the cytoplasm of red blood cells is composed of hemoglobin). The final problem with this method is that the Stokes radius of the probe molecule needs to be known and the determination of this is not straightforward.[5] In the PFG method, the attenuation of a spinecho signal resulting from the dephasing of the nuclear spins due to the combination of the translational motion of the spins and the imposition of spatially well-defined gradient pulses is used to measure motion. In contradistinction to the relaxation method, no assumptions need to be made regarding the relaxation mechanisms, or in relating τ_c to the translational motion of the probe molecule. However, to determine the "true" diffusion coefficient, D, as against an "apparent" diffusion coefficient D_{app} the effects

of structural boundaries that affect the natural diffusion of the probe species need to be considered. The mathematics required to model anything except for free diffusion or diffusion within simple geometries becomes rather complicated, and as a result, analytical solutions are generally not possible and numerical solutions must be sought.[5]

1.5 Nanoparticles

Nano science plays an important role in the study of biological phenomenon because the size of inorganic nanoparticles as probes and the spatial resolution of nanotools match the sizes of macromolecules.[6]Nanosystems can be prepared in a variety of shapes. Nanocrystals are often irregular; there are asymmetric carbon nanotubes, and surfactant and lipid vesicles can be produced as discs, polyhedral structures, toroids and tubes. The vesicles constructs often have dimensions larger than 500 nm; it must be assumed that vesicles in the nanometer size range will be less affected. In these systems, shape is less important than membrane properties in controlling the release of encapsulated drug, but the flow properties of vesicular suspensions are clearly determined by shape and elasticity. [6]

Polymeric nanoparticles are promising vehicles for site-specific and controlled delivery of therapeutic agents, following different routes of administration and these trends seem to continue with advances in materials and polymer chemistry and pharmaceutical nanotechnology. However, nanoparticle do not behave similarly; their encapsulation capacity, drug release profile, biodistribution and stability vary with their chemical makeup, morphology and size. Inherently, nanosphere design and targeting strategies may vary according to physiological and therapeutic needs, as well as in relation to the type, development stage and location of the disease. Attention should also be paid to toxicity issues that may arise from nanoparticle administration and the release of their polymeric contents and degradation products.

1.6 Triblock Copolymer

Copolymers are derived from two(or more) type of monomeric species. Block Copolymers are polymers of copolymers with block of these monomeric species. Triblock Copolymer has a block of 3 monomeric species to polymerize. In our studies we used Polyethylene Glycol(PEG)-Polypropylene Glycol(PPG)-Polyethylene Glycol(PEG) as a block. Triblock Copolymers(PEG-PPG-PEG) are quite useful because of their property of forming Self-Constructing Meshes. By varying the concentration of Triblock Copolymers we can change the mesh properties. These meshes can be used as a vesicles for nanoparticles for possible drug delivery applications.

1.7 Lipid Membrane Mimetics

All cells are bounded by a thin membrane called the *plasmalemma*. This membrane is not visible under the light microscope. The structure seen under the light microscope is the *cell membrane*. This consists of the plasmalemma along with surrounding *cell cement*.

In an attempt to explain the physical and biological features of cell membranes two main categories of hypotheses have been proposed, the *bilayer models* and the *micellar* or *subunit models*. In the *bilayer models* the protein and lipid constituting the membrane are believed to occur in layers. In the *micellar model* the membrane is believed to consist of a number of similar units.[7–9]

Membranes being 5 to 8 nm (50 to 80 $\mathring{A}$) thick are only permeable to nonpolar compounds, The physical studies of permeability and the motion of individual protein and lipid molecules within membranes and combined evidence from electron microscopy and studies of chemical composition, led to the development of the **fluid mosaic model** for the structure of biological membranes.[9] Phospholipids form a bilayer in which the nonpolar regions of the lipid molecules in each layer face the core of the

bilayer and their polar head groups face outward, interacting with the aqueous phase on either side. "Sidedness" of the bilayer is determined by the protein which are embedded in this bilayer sheet, held by hydrophobic interactions between hydrophobic domain of proteins and membrane lipid. Some of these proteins protrude from only one side of the membrane; others have domains exposed on both sides. The orientation and functional behavior of proteins in the bilayer is asymmetric, which determines the sidedness of the membrane. The individual lipid and protein units in a membrane form a fluid mosaic with a pattern that, unlike a mosaic of ceramic tile and mortar, is free to change constantly.[7] The membrane mosaic is fluid because most of the interactions among its components are noncovalent, leaving individual lipid and protein molecules free to move laterally in the plane of the membrane. We now look at some of these features of the fluid mosaic model in more detail and consider the experimental evidence that supports the basic model but has necessitated its refinement in several ways.[7–9]

1.7.1 Bilayer Models

In 1895 Overton found that fat-soluble substances passed easily through the cell membrane. He therefore concluded that the cell membrane contained lipids. Later Hober(1910) and Fricke(1925) found that the intact cell had low electrical conductivity, indicating a lipid bilayer. The existence of a lipid layer was confirmed on the basis of experience.[7]

Glycerophospholipids, sphingolipids, and sterols are virtually insoluble in water. When mixed with water, they spontaneously form microscopic lipid aggregates in a phase separate from their aqueous surroundings, clustering together, with their hydrophobic moieties in contact with each other and their hydrophilic groups interacting with the surrounding water. Lipid clustering reduces the amount of hydrophobic surface exposed to water and thus minimizes the number of molecules in the shell of ordered water at the lipid-water interface, resulting in an increase in entropy. Hydrophobic

interactions among lipid molecules provide the thermodynamic driving force for the formation and maintenance of these clusters. Depending on the precise conditions and the nature of the lipids, three types of lipid aggregates can form when amphipathic lipids are mixed with water. [7–9] A first type of lipid aggregate in water is the **bilayer**, in which two lipid monolayers (leaflets) form a two-dimensional sheet. Bilayer formation occurs most readily when the cross-sectional areas of the head group and acyl side chain(s) are similar, as in glycerophospholipids and sphingolipids. The hydrophobic portions in each monolayer, excluded from water, interact with each other. The hydrophilic head groups interact with water at each surface of the bilayer. Because the hydrophobic regions at its edges are transiently in contact with water, the bilayer sheet is relatively unstable and spontaneously forms a third type of aggregate: it folds back on itself to form a hollow sphere, a vesicle or **liposome**. By forming vesicles, bilayers lose their hydrophobic edge regions, achieving maximal stability in their aqueous environment. These bilayer vesicles enclose water, creating a separate aqueous compartment. It is likely that the precursors to the first living cells resembled liposomes, their aqueous contents segregated from the rest of the world by a hydrophobic shell.[7–9]

1.7.2 Lipid Bilayer Gel Phase Transition

Amphiphilic phospholipids, a major constituent of biological membranes, are involved in numerous cell activities, ranging from simple mechanical functions to complex and highly specific biomolecular interactions. The thermodynamic and structural behavior of the lipid membrane depends strongly on its chemical environment and composition. Fundamental understanding of this dependence is necessary for the development of lipid-based technologies, e.g., drug delivery and biological sensors. [10] One of the properties that greatly influences membrane functionality and behavior is the phase state of the lipid bilayer.It is well established that one-component saturated lipid bilayers undergo a reversible transition between an ordered gel phase and a disordered

liquid-crystalline phase at a specific temperature termed the main chain transition temperature. The structural properties of the gel and liquid crystalline phases are significantly different, bringing about a dependence of the bilayer's functionality on its phase state. [10]

The presence of an adsorbed particle could affect the molecular conformations of the phospholipid molecules and change the structural properties of the fluid-like bilayer. Consequently, essential biological functions of the phospholipid membrane could be inhibited. For instance, membrane fluidity, which is characterized by the relative motional freedom of the lipid molecules within the plane of the bilayer, is a central property that is present in the liquid-crystalline phase but not in the gel phase.[11] Changes in membrane fluidity have been associated with changes in the functionality of the bilayer, including enzyme activity and ligand receptor interactions. Their experimental evidence[12] suggests that when negatively charged nanoparticles are adsorbed onto a dipalmitoylphospha- tidylcholine (DPPC) bilayer, which has zwitterionic head-groups, there is an induced ordering of the bilayer and the lipid molecules undergo a phase transition. These experiments demonstrate how changes in the environment around the phospholipid bilayer can have a significant effect on its behavior. [11, 12]

1.7.3 Chemistry of DPPC

- Biological membranes define cellular boundaries, divide cells into discrete compartments, organize complex reaction sequences, and act in signal reception and energy transformations.

- Membranes are composed of lipids and proteins in varying combinations particular to each species, cell type, and organelle. The fluid mosaic model describes features common to all biological membranes. The lipid bilayer is the basic structural unit. Fatty acyl chains of phospholipids and the steroid nucleus of

sterols are oriented toward the interior of the bilayer; their hydrophobic interactions stabilize the bilayer but give it flexibility.

- Peripheral proteins are loosely associated with the membrane through electrostatic interactions and hydrogen bonds or by covalently attached lipid anchors. Integral proteins associate firmly with membranes by hydrophobic interactions between the lipid bilayer and their nonpolar amino acid side chains, which are oriented toward the outside of the protein molecule.[7]

- Some membrane proteins span the lipid bilayer several times, with hydrophobic sequences of about 20 amino acid residues forming transmembrane α helices. Detection of such hydrophobic sequences in proteins can be used to predict their secondary structure and transmembrane disposition. Multistranded β barrels are also common in integral membrane proteins. Tyr and Trp residues of transmembrane proteins are commonly found at the lipid-water interface.

- The lipids and proteins of membranes are inserted into the bilayer with specific sidedness; thus membranes are structurally and functionally asymmetric. Many membrane proteins contain covalently attached oligosaccharides. Plasma membrane glycoproteins are always oriented with the carbohydrate-bearing domain on the extracellular surface.[7]

1.8 Organization of the Thesis

This thesis is organized as follows: Chapter 2 talks about basics of diffusion and finding diffusion constants using NMR. Chapter 3 discusses the basics and previous studies of nanoparticles and some of our experimental results of NMR of silver nanoparticles are also presented. Chapter 4 deals with the interaction of silver nanoparticles with **D**i **P**almitoyl **P**hosphatidyl **C**holine(DPPC) bilayer. Gel to Liquid phase transitions and consequences of temperature have been experimentally observed using ^{31}P NMR.

Chapter 5 deals with experimental studies of interactions between silver nanoparticles and triblock copolymers. Chapter 6 contains the concluding remarks and an outlook for the future.

Chapter 2

Diffusion Studies Using PFG NMR

2.1 Diffusion

Diffusion can be understood as motion of a Random Walker e.g. Pollen grains. Einstein said, although we can not see the small rapid jerks of the pollen grains due to individual molecular collision still we can and will see the rare large displacements. Random walk has structure on all length scales. For **1D** one can visualize a random walk by tossing a coin once per second & each time you get heads, you move the marker one step to the east; for tails, one step to the west. Once in a while you will flip 100 heads in a row thus producing a step clearly visible from after. For **2D** place the marker on the checkerboard and flip two coins each second: use the first coin to move the marker east/west and use the second coin to move the marker north/-south. The path traced by marker is then a two-dimension random walk; each step is a diagonal across a square of a checkerboard.

2.1.1 Diffusion Law

Diffusion law is model independent. Diffusion law is universal as long as we have some distribution of random, independent steps. Suppose each step is of length L. Thus the displacement of step j is k_jL , where k_j is equally likely to be ± 1. Call the position after j steps x_j with initial condition $x_0 = 0$

$x_1 = k_1L$

$x_j = x_{j-1} + k_jL$

$\langle (x_N)^2 \rangle = \langle (x_{N-1} + k_NL)^2 \rangle = \langle (x_{N-1})^2 \rangle + 2L\langle k_N x_{N-1} \rangle + L^2 \langle k_N \rangle^2$

$\langle (x_N)^2 \rangle = NL^2$

If we wait a total time t then the marker makes $N = t/\triangle t$ random steps and diffusion constant $D = L^2/2 \triangle t \Rightarrow L^2 = 2D \triangle t \Rightarrow NL^2 = 2Dt$. Thus for one dimension

$$\langle (x_N)^2 \rangle = 2Dt \tag{2.1}$$

In this case any individual walk will not conform to diffusion law even approximately. There are few steps which we need to follow in order to calculate diffusion constant for a colloidal particle:

1. Note the initial position of colloidal particle.
2. Wait a time t
3. Note final position
4. Calculate $x^2/2t$
5. Make several observations
6. Average of $x^2/2t$ gives D
7. Value of D thus found will not depend on elapsed time t

Suppose our marker steps of various lengths. We are given a set of numbers P_k, the probabilities of taking steps of length k_L, where k is an integer length k_j of step j can be positive or negative. Relative probabilities of the various step sizes are all the same for each step. So $u = \langle K_j \rangle = \Sigma k_{P_k}$ average drift motion superimposed on the random walk

$\langle x_N \rangle = \langle x_{N-1} \rangle + L\langle k_N \rangle$

$= \langle x_{N-1} \rangle + uL$

$= NuL$

Diffusion concerns the fluctuation about the mean thus we have to compute the variance (mean square deviation)

variance$(x_N) = \langle (x_N - \langle x_N \rangle)^2 \rangle$

$= \langle (x_{N-1} + k_N L - NuL)^2 \rangle$

$= \langle ((x_{N-1} - u(N-1)L + (k_N L - uL))^2 \rangle$

$= \langle (x_{N-1} - u(N-1)L)^2 \rangle + \langle (k_N L - uL)^2 \rangle + 2\langle (x_{N-1} - u(N-1)L)(k_N L - uL) \rangle$

$= \langle (x_{N-1} - u(N-1)L)^2 \rangle + L^2 \langle (k_N - \langle k_N \rangle)^2 \rangle$

$= variance(x_{N-1}) + L^2 variance(k)$

After N steps, variance is $NL^2 * variance(k)$ so $variance(x_N) = 2Dt$,

$\Rightarrow D = (L^2/2\Delta t) variance(k)$. If there is no drift u=0 then $D = L^2/2\Delta t$ and this implies that diffusion law is model independent.

Similarly for **2D walk** on checkers board with squares of side L gives diffusion constant as $D = L^2/2 \triangle t$ and now each step is diagonal and hence has length $L\sqrt{2}$ so $\langle (r_N)^2 \rangle = \langle (x_N)^2 \rangle + \langle (y_N)^2 \rangle = 4Dt$ is twice as large as before. **For 3D** the expressions is $\langle (r_N)^2 \rangle = 6Dt$.

2.2 Fick's Law

In terms of concentration in number of particles per unit volume, c(r,t), the flux of a particle is given by Fick's first law of diffusion

$$J(r,t) = -D\nabla c(r,t) \tag{2.2}$$

The minus sign indicates that(in isotropic media) the direction of flow is from larger to smaller concentration. Because of the conservation of mass, the continuity theorem applies, and thus,

$$\frac{\partial c(r,t)}{\partial t} = \nabla . J(r,t) \tag{2.3}$$

This equation states that $\partial c(r,t)dt$ is the difference between the flux and efflux from the point location at r. Combining above equations we arrive at Fick's second law of diffusion:

$$\frac{\partial c(r,t)}{\partial t} = -D\nabla^2 c(r,t) \tag{2.4}$$

2.3 Stejskal-Tanner Equation

$$\ln(\frac{S(k)}{S(0)}) = -D(\gamma\delta g)^2(\Delta - \frac{\delta}{3}) \tag{2.5}$$

where:

$S(k)$ is intensity of signal in the presence of field gradient pulse

$S(0)$ is intensity of signal in the absence of field gradient pulse

D is diffusion Coefficient

γ is gyromagnetic ratio

δ is duration of field gradient pulse

Δ is diffusion delay time

g is field gradient strength

2.4 Stokes-Einstein Equation

:

$$D = \frac{kT}{f} \tag{2.6}$$

where frictional coefficient $f = 6\pi\eta R_h$

η is viscosity

R_h is hydrodynamic radius

D is Diffusion Coefficient

k is Boltzmann Constant

T is Temperature

2.5 Diffusion NMR

The molecular translation in the solution arises due to molecular thermal energy. This translational motion is known as Brownian molecular motion and is called diffusion or self diffusion. It depends on various physical parameters like size and shape of the molecule, temperature and viscosity. The diffusion coefficient is given by Stokes-Einstein equation as

$$D = \frac{kT}{6\pi\eta r_s} \tag{2.7}$$

where k is the Boltzmann constant, T is the temperature, η is the viscosity of the liquid and r_s is the hydrodynamic radius of the molecule (it is assumed that the molecule is having spherical shape). This self-diffusive motion can only be detected by various methods. Nuclear magnetic resonance provides a molecular label via the

characteristic Larmor frequencies of the component nuclei. This label may be given a spatial dependence by the imposition of a well defined magnetic field gradient over the sample space. The suggestion that spin echo signals might be used to measure molecular translational motion was first given by Hahn (1950) when he proposed the spin-echo (SE) experiment. A precise theoretical treatment of this sequence was provided by Carr and Purcell (1954). All NMR diffusion measurements are based on the fact that the diffusion coefficient can be calculated from the echo attenuation if the amplitude and duration of magnetic field gradient are known. Magnetic field gradients are produced using quadrupolar coils [13], as they are superior in their geometry, have smaller inductance/gradient ratio and the ease with which orthogonal independent $\partial B_o/\partial x$ and $\partial B_o/\partial z$ gradients are incorporated in one assembly. Protons offer the greatest sensitivity in NMR because of their high gyromagnetic ratio, although PFGNMR experiments have been reported using ^{13}C, ^{2}H, ^{19}F and ^{7}Li [14, 15].

2.5.1 Diffusion ordered NMR spectroscopy (DOSY)

Diffusion can be obtained by incrementing the areas of the gradient pulses (q) in PFGNMR. The result is diffusion ordered NMR spectroscopy (DOSY). The three basic DOSY requirements are (i) distortion free absorption mode data sets acquired with precise gradient encoding, (ii) effective data inversion (transformation) procedures, and (iii) algorithms for the display of the diffusion spectra. DOSY requires high quality gradient probes which incorporate active shielding and are designed to provide constant (flat) gradients over the NMR active sample volume.

2.5.2 Pulse sequence

The pulse sequence mostly used for DOSY experiment is stimulated echo (STE) sequence show in Figure 2.1. This sequence consists of three 90°rf pulse which can generate up to five echoes. The advantages of the STE sequence arise because the

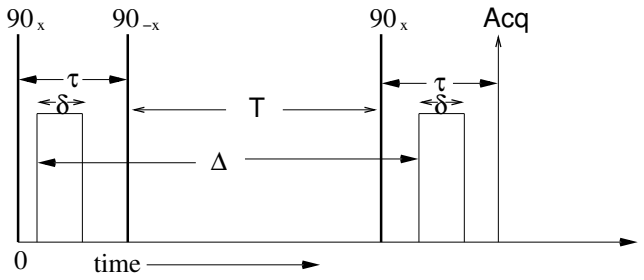

FIGURE 2.1: Stimulated Echo(STE) pulse sequence to measure diffusion coefficient in a DOSY experiment

evolution time for transverse magnetization can be limited. When $2\tau \ll T$, spin relaxation starts depending on T_1 rather than T_2, and with $\tau \ll 1/J$, J-modulation is not signi[U+FB01]cant. The advantage of T_1 relaxation relative to T_2 relaxation depends on the ratios R=T_2/T_1 and X=T/T_1. For T $\cong \Delta$ and $T \gg \tau$ the STE/SE signal ratio will be given by $(0.5)\exp[R(X-1)/X]$ for R=0.1 and X=0.5 the enhancement factor is greater than 200. But the problem is gradient pulses tend to induce eddy currents in the surrounding metal structures of the probe and the magnet. These eddy currents in turn produce slowly decaying magnetic fields at the sample that lead to spectral distortions resulting from time dependent phase changes. Therefore, experiments must be designed which avoid or at least minimize the effects of eddy currents. There is also the related requirement that the NMR resolution can be maximized to avoid overlap of peaks from different components in a mixture as data transformations, required to produce diffusion spectra, fail when NMR peaks for similar sized molecules overlap.

The best way to avoid the effects of eddy currents is to prevent its formation. There are some ways but not very effective. In spite of the best efforts, eddy current effects are still significantly and they depend on the strength of the gradient pulses. The stimulated echo (see Fig. (2.2)) is primarily affected by eddy currents induced by the final gradient pulse, and the problem can be solved by keeping τ short in order to minimize transverse relaxation and J- modulation. One more pulse sequence called Longitudinal Eddy-current Delay (LED) sequence is also now a days being used quite widely in which the major change is the addition of a fourth 90°pulse at the center of

the stimulated echo for the purpose of storing the magnetization in the longitudinal direction while the eddy currents decay. After the eddy current settling period T_e, the magnetization is recalled with a fifth 90°pulse and the FID is acquired. The effectiveness of this sequence is further enhanced by adding three gradient pre-pulses to make a chain of five equally spaced pulses.

The LED sequence significantly improves the quality of spectra but suffers from the slowly decaying eddy currents. The consequence is that the T_e period, required to obtain undistorted spectra in experiments with large gradient pulses, can be unacceptably long. There is also the problem that the gradient pre-pulses introduce additional heat.

One of the best ways to diminish the eddy currents induced by a short gradient pulse (g) is to replace the pulse with two pulses of different polarity separated by a 180°RF pulse, i.e. the composite bipolar gradient pulse combination (g-180°-(- g)). Gradient pulse sequences with alternating polarity were introduced into PFG-NMR by Karlicek and Lowe(1980) to take advantage of the fact that the 180°RF pulses refocus static gradients. A number of STE sequences were proposed with alternating grading polarities to minimize the effect of background gradients. More recently all of the gradient pulses in the LED sequence were replaced with bipolar pulse pairs (BPPs) to permit diffusion measurements in the presence of large background gradients. The BPPs were found to cancel more than 95% of the eddy currents, and undistorted signals could be obtained with T_e reduced by a factor of 20. Further, this improvement could be obtained without the need for gradient pre-pulses, thus reducing undesirable heating effects.

Eddy current compensation is more complete when both δ and τ are short. The extra introduced 180°pulses cause some loss of signal because of the greater sensitivity to inhomogeneities in the RF pulses. However, this turns out to be an advantage because signal acquisition is limited to the region where the gradient is constant and higher quality data result. Also, the refocusing effect of the 180°pulses does eliminate the

effect of steady background gradients, and more importantly for DOSY it refocuses chemical shifts. The latter can be very important when chemical exchange or spin diffusion is present. At present the BPP-LED sequence is the sequence of choice for many DOSY experiments, especially those requiring maximum gradient strengths with small temperature rises. It can also be combined with water suppression sequences if required.

2.6 Diffusion Analysis

2.6.1 Method for discrete diffusion coefficient(SPLMOD)

SPLMOD is a single channel method which is restricted to analyse a system with discrete diffusion coefficients. SPLMOD intends to analyse sums of pure exponentials by performing least square fit of

$$S(\nu, t) = \sum_{i=1}^{n} S_0(i) \exp(-\lambda_i s) + E \tag{2.8}$$

where n is the number of components, $\lambda = D(i)(\Delta - \delta/3)$, $s = K^2$, $K = \gamma g \delta$ and E accounts for noise. S is the intensity of a specific frequency channel ν and its variation of exponential decaying depends on the increase of s. Resolution of discrete components using SPLMOD with certain rejection criteria has been presented by Morris and Johnson([17]). However, with the benefit of remedial constraints, SPLMOD still suffers from the overlap problem, i.e. It is difficult to separate more than two components in one single channel. It is also very sensitive to noise and hence SPLMOD often overestimates the number of the components.[18]

2.6.2 Method for continuous diffusion coefficients (CONTIN)

Some samples are composed of components with continuous distributions of diffusion coefficients, e.g. Polymers and aggregates. For a specific frequency channel of the data of polydisperse system, the signal can be described by:

$$S(\nu, t) = \int_{min\lambda}^{max\lambda} g(\lambda) \exp(-\lambda s) d\lambda + E \tag{2.9}$$

$g(\lambda)$ represents the 'spectrum' of diffusion coefficients and can be obtained by an inverse laplace transform(ILT). A method called CONTIN, a constrained regularization program, attempts to solve this ILT problem and obtain the Laplace spectrum of the

diffusion coefficients. The constraints are based on the non-negativity of the signal and decay constant, statistical prior knowledge and parsimony. Usually, the smoothest solution with the minimum number of peaks is selected. There is no need to provide the number of components and only the threshold value is chosen as input for the program. An advantage of CONTIN is that it allows broad and narrow distributions and therefore it can be used to analyse an unknown system without any knowledge of whether the diffusion coefficient follow discrete or continuous distribution. If the distribution is narrow, then it can be reanalysed by SPLMOD if desired. The major problem is caused by essential smoothing features which broaden all the peaks, even those of monodisperse components. This problem can lead to two monodisperse components to be described by one continuous diffusion coefficient. Thus, CONTIN often presents an incorrect number of components, due to oversmoothing. Other limitations of CONTIN include the requirement of high S/N. [18]

2.6.3 Direct exponential curve resolution algorithm (DECRA)

DECRA is a multivariate method to calculate the pure spectrum and the corresponding decay profile of each component based on the GRAM.

DECRA is a fast algorithm to obtain information of pure component in a mixture. It can deal with spectra with overlapping regions within a few seconds. DECRA requires equally spaced gradient(g^2) to create exponential decay data. This is easy to implement experimentally. However, in the experimental data, the increase of g^2 can be non-linear due to the systematic error. Therefore, even if the experiment parameters are set to fulfill the requirement of getting equally spaced g^2, it is recommended that non-linear g^2 levels be checked and corrected before using the DECRA. The limitation of DECRA is that it can only be applied to discrete diffusion components with the range of about two orders of magnitude in the diffusion dimension due to the requirement of equal g^2 steps.[18]

Chapter 3

NMR of Nanoparticles

3.1 Introduction

Fast developing nanotechnology, among other areas, is expected to have a dramatic impact on medicine. The application of nanotechnology for treatment, diagnosis, monitoring, and control of biological systems has recently been labeled as nanomedicine. Among the approaches for exploiting nanotechnology developments in medicine, various nanoparticles offer some unique advantages as pharmaceutical delivery systems and image enhancement agents. Several varieties of nanoparticles are available: different polymeric and metal nanoparticles, liposomes, micelles, quantum dots, dendrimers, microcapsules, cells, cell ghosts, lipoproteins, and many different nanoassemblies. All these nanoparticles can play a major role in diagnosis and therapy. [19]

Among particulate drug carriers, liposomes, micelles and polymeric nanoparticles are the most extensively studied and possess the most suitable characteristics for encapsulation of many drugs and diagnostic agents. Making these nanocarriers multifunctional and stimuli-responsive can dramatically enhance the efficiency of various drugs carried by these carriers. These functionalities are expected to provide:

- prolonged circulation in blood and the ability to accumulate in various pathological areas(such as solid tumors) via enhanced permeability and retention effect (EPR effect)
- ability to specifically recognize and bind target tissues or cells via the surface-attached specific ligand.
- ability to respond local stimuli characteristic of the pathological site by, for example, releasing an entrapped drug or specifically acting on cellular membrane under abnormal pH or temperature in disease sites
- ability to penetrate inside cells by passing the lysosomal degradation for efficient targeting of intracellular drug targets

Hydrophobicity and low solubility in water appear to be intrinsic properties of many drugs, since it helps a drug molecule to penetrate a cell membrane and reach important intracellular targets. By the virtue of small size and by functionalizing their surface with synthetic polymers and appropriate ligands, nanoparticles carriers can be targeted to specific cells and locations within the body after intravenous and subcutaneous routes of injection. [20]

3.2 Utility and Application of AgNPs

- Silver is an effective antimicrobial agent with low toxicity.
- Drug releasing silver in ionic forms are known to get neutralized in biological fluids and upon long-term use may cause cosmetic abnormality e.g. argyria and delayed wound-healing.
- Silver nano particle have been the focus of increasing interest.
- It is an excellent candidate for therapeutic purposes.

- Nano-delivery systems are attractive to researcher because of their ability to efficiently penetrate tumors and eliminate them in a single treatment.
- Nano particle have the potential to cross the blood brain barrier and this may open new ways for drug delivery into the brain. [21]
- Access into the cell and various cellular compartments including nucleus.

3.3 Previous NMR Studies of NP

A study of gold nanoparticles(NPs) by Canzi et al. [22]presents a time and cost effective way to characterize alkanethiol protected Au nanoparticles via 2D diffusion based NMR. 2D NMR has been used to study nanomaterials in multitude of ways recently, including ligand exchange kinetics of organic bound to NP surfaces, along with composition and purification of nanomaterials.[23, 24] 2D diffusion-ordered NMR(DOSY) spectroscopy has previously been used as an effective tool in bridging imaging and species characterization.[25, 26] The technique is especially powerful when dealing with mixtures containing large distribution of particle size, as is often the case in nanoparticle studies. Using 2D DOSY NMR, size estimates of varying length alkanethiol protected nanoparticles were obtained using correlated diffusion coefficients of nanoparticle capping thiols as referenced to an internal standard[27]. A significant finding by this group is that protecting thiols do not have direct effect on hydrodynamic radii of nanoparticles in the solvents studies, and thus the measurements obtained from DOSY were in direct agreement with other visual measurements from TEM and were a true estimate of the metal core size.[27, 28]

In another study Gomez et al.[29] have reported a new method for measuring the size of metal nanoparticles encapsulated within dendrimers. This approach should be appropriate for measuring the size of any encapsulating object as long as the following two conditions are met. First, the host must have a regular structure. Second, the

guest must affect a property of the host in a way that can be detected by NMR. The advantage of this method for dendrimer-encapsulated nanoparticle(DEN) system are the remarkable sensitivity of proton resonances to nanoparticle size and the fact that the average nanoparticle size can measured in situ. So a straightforward 1D 1H NMR experiment can be used to readily distinguish between DENs differing in size by just a few tens of atoms.

3.4 Materials & Method

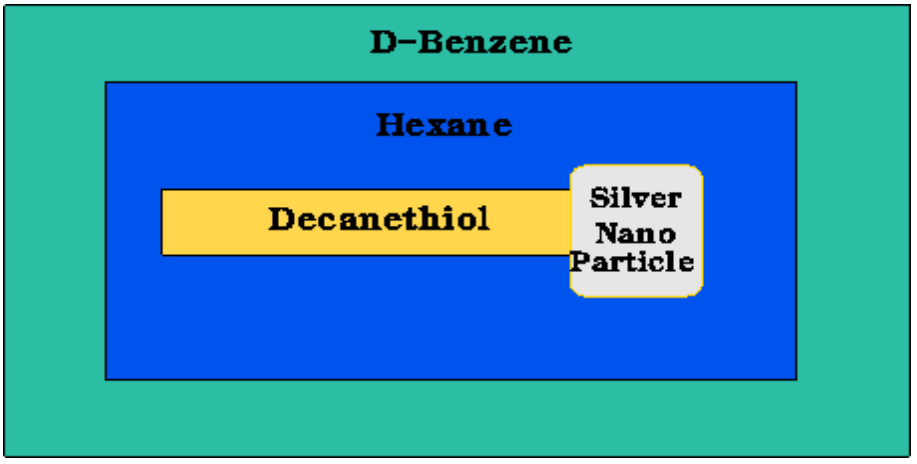

FIGURE 3.1: Silver Nano Particle System

Various functional groups can be easily introduced onto the nanoparticle surface for mediating both the nanoparticles solubility and serving as a point of chemical attachment for biomolecules. Biofunctional ligands may be used which present a surface anchoring moiety to bind to the inorganic nanoparticle(for example, thiol) and an opposing hydrophilic end group(for example, hydroxyl, carboxyl) to achieve water compatibility. Once the nanoparticle surface has been modified, biomolecules such as proteins, enzymes, antibodies, oligonucleotides can be linked to the nanoparticle following standard conjugation protocol. Silver Nano Particle were substrated on Decanethiol and this whole system(3.2) was dispersed in hexane solvent for stability. This system of Silver Nanoparticle was purchased from Sigma Aldrich. Various

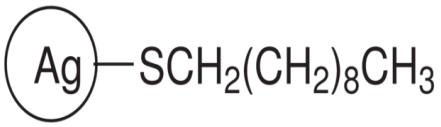

FIGURE 3.2: Silver Nanoparticle with it's substrate Decanethiol

solvents were used to check compatibility of the system like DMSO, Ethanol & D-Benzene mixure, D_2O and D-Benzene. D-Benzene gave the best spectra because of its nonpolar nature. Its compatibility with hexane is the most. The effect of silver nanoparticles on substrate were also checked (Decanethiol was also purchased from Sigma Aldrich)

3.5 Results and Analysis

Decanethiol in D-Benzene solvent 1H Spectra(Figure 3.3(a)) showing one extra peak of proton connected to Sulpher in thiol group. Decanethiol+Hexane in D-Benzene(Figure 3.3(b)) has the same spectra as Figure 3.3(a) except the width of signal at around 0.89 & 1.23. These being standard 1H peak for hexane in D-Benzene. Silver Nanoparticle(silver capped decanethiol dispersed in hexane) in D-Benzene 1H Spectra(Figure 3.3(c)) which does not have thiol proton peak and also all other proton peaks are coming in spectra due to asymmetric electronic environment created by the presence of Silver Nanoparticles.

Similarly ^{13}C Spectra of Silver Nanoparticle+D-Benzene(Figure 3.4(c)) is quite sim-

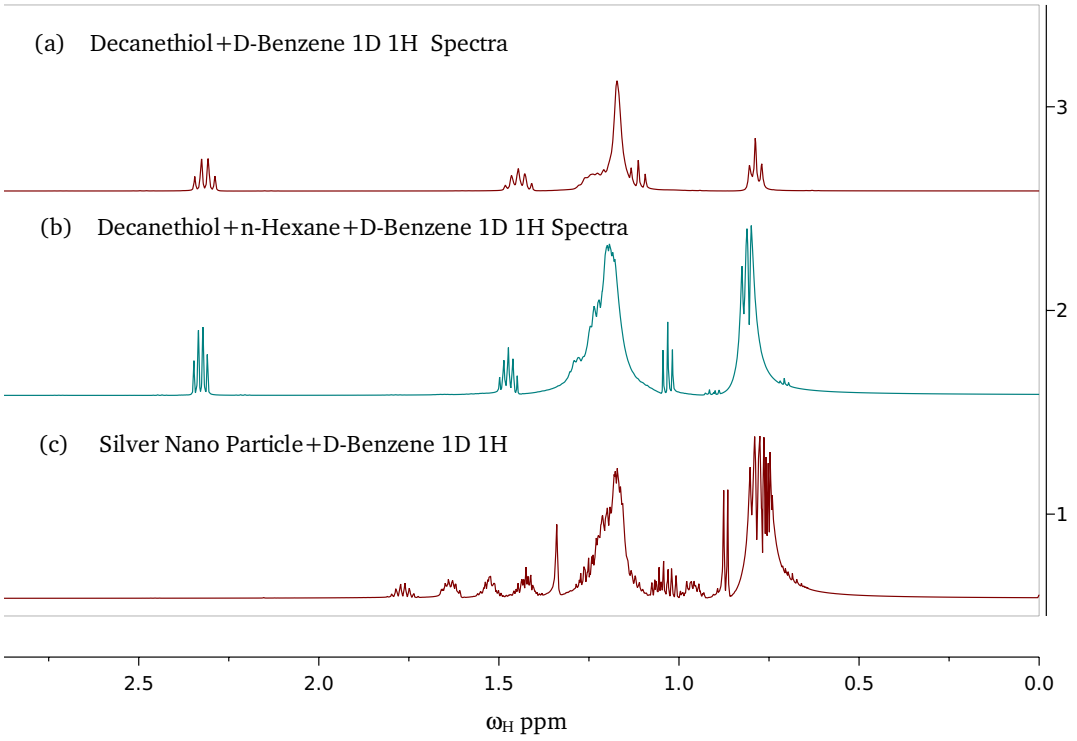

FIGURE 3.3: (a) Decanethiol in D-Benzene 1H Spectra (b) Decanethiol+Hexane in D-Benzene (c) Silver Nano Particle(silver capped decanethiol dispersed in hexane) in D-Benzene 1H Spectra

ilar to Decanethiol+Hexane+D-Benzene(Figure 3.4(b)) except some peaks of carbon due to asymmetry generated because of silver. In the case of carbon spectra there are no thiol carbon so that peak will not come into the picture here.

2D COSY NMR spectra of Silver Nanoparticle+D-Benzene is very different from the Decanethiol+Hexane+D-Benzene is due to the same asymmetry in the chemical environment generated by silver in silver nanoparticle system(3.2). We can clearly see the correlations exists in Figure 3.5(a,b) due to thiol protons, but it is absent in Figure 3.5(c) because that proton is replaced with silver here.

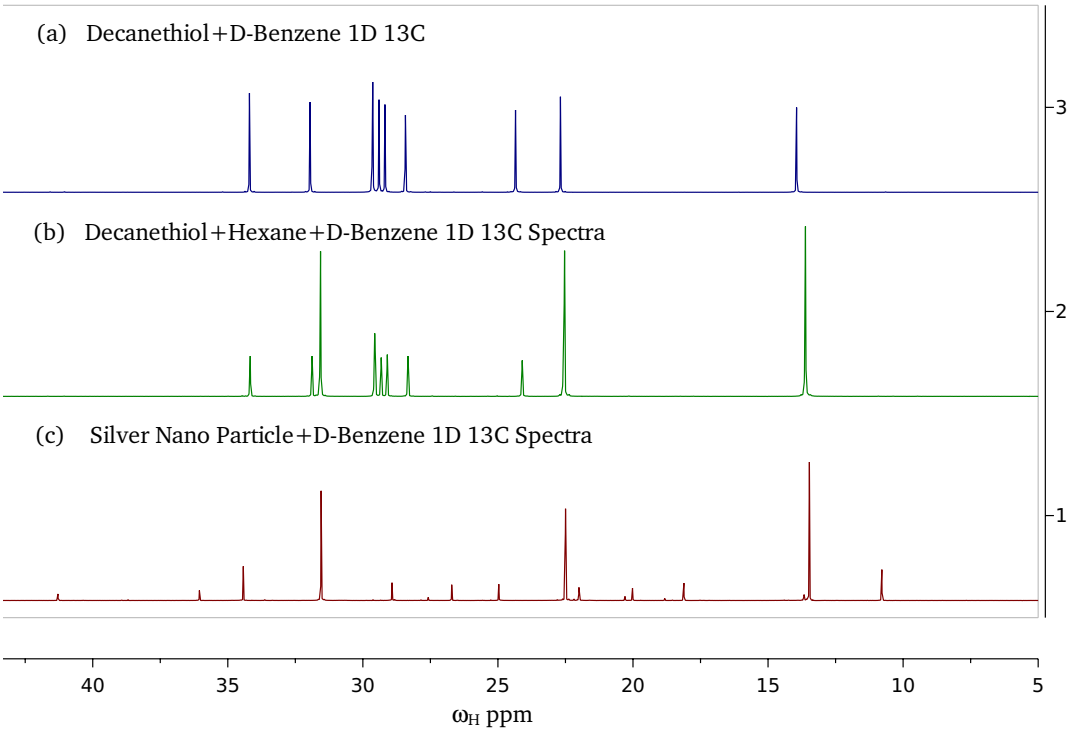

FIGURE 3.4: (a) Decanethiol in D-Benzene solvent ^{13}C Spectra (b)^{13}C Spectra of Decanethiol+Hexane in D-Benzene (c) Silver Nanoparticles(silver capped decanethiol dispersed in hexane) in D-Benzene ^{13}C Spectra

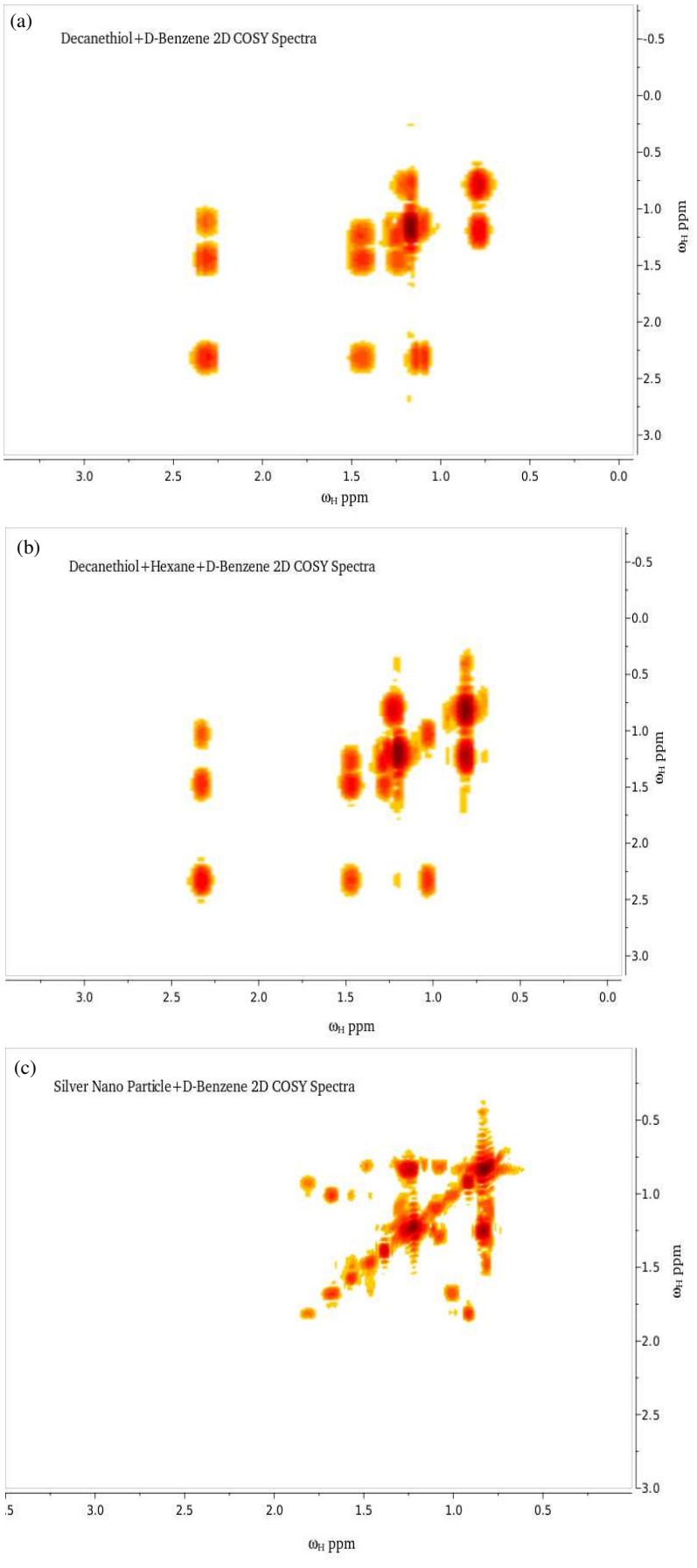

FIGURE 3.5: 2D COSY Spectra of (a) Decanethiol+D-Benzene, (b)Decanethiol+Hexane+D-Benzene and (c) Silver Nanoparticles+D-Benzene.

Chapter 4

Permeation of AgNPs in Lipid Bilayer

4.1 Introduction

Recent advances in the available experimental techniques to synthesize nanoparticles from a variety of starting materials and with well controlled geometry, size distribution, and surface chemistry has opened new unprecedented opportunities[3] in using these nano particles for drug delivery, imaging, and as antimicrobial agents. Rational design of multifunctional nanoparticles with programmable functionalities require fundamental understanding of how they interact with lipid membranes. Experimental studies in the field report a number of possible mechanisms of interaction between nanoparticles and lipid membranes. These mechanisms depend on the morphology of nanoparticles(size, shape), surface chemistry, and charge, as well as the characteristics of the environment, including type of cell membrane, pH, and interaction with other biological entities present in the system. [3]

Hybrid lipid/nanoparticle conjugates provide a biologically inspired means of designing stable agents for biomedical imaging, drug delivery, targeted therapy, and biosensing. An advantage of using lipids as stabilizing of functional ligands is that they mimic the lipid scaffolding of biological membranes and have well-characterized physicochemical membranes and phase behavior. In lipid vesicles, nanoparticle encapsulation can be achieved by trapping particles within the aqueous vesicle core or within the hydrophobic lipid bilayer. To embed nanoparticles within lipid bilayers, the nanoparticle must be small enough to fit within a DPPC bilayer and it must present a hydrophobic surface. For hydrophobic nanoparticles embedded within lipid bilayer, which is the focus of this work, the presence of nanoparticles can lead to changes in lipid packing and may disrupt lipid-lipid interactions amongst the head group and/or acyl tails. Disruption of such inter-lipid interactions can result in changes in lipid bilayer phase behavior, which is related to the degree of lipid ordering and bilayer viscosity. Hence, depending on their size and surface chemistry, embedded nanoparticles may influence the stability and function of hybrid vesicle, as well as the conditions required for preparation. [2]

Since nanoparticles(NPs) that are capable of crossing cellular barriers can migrate into systemic circulation, attention is given to factors that influence the permeation process. Additionally, the presence of trapped, hydrophobic NPs can instigate changes in lipid packing and influence the phase behavior of the bilayer. Reciprocally, the permeability of molecular NPs into lipid bilayers themselves, as well as the morphology and polarity of permeant molecules. A clear difference in the permeation of small molecules like NPs has been shown by computational simulation and calculation of so-called local diffusion constant as a function of permeant depth z, within the bilayer. NP diffusion constant values, however, have been observed to be relatively independent of molecular position in bilayer interior.[1]

Liposome is the assembling structure that cell membrane like lipid dispersion from bilayers spontaneously in water. Liposome exhibits many features of the surface of which acts as a permeability barriers and the fluidity of lipid membranes plays a very

important role for the cell. These liposomes can mimic various functions of biological membranes and can be used as a container for storage, transport and controllable release of compound; therefore, it is widely used in drug delivery system. It has been known that liposome can be constructed with bilayer permeability responsive to a variety of physical and chemical stimuli, including temperature, light, pH, and ions. On the other hand, nanoparticles that consist of metals such as silver, gold, and palladium seem to be attractive units for the engineering of such structures. Nano materials such as metal nanoparticles exhibit similar dimensions to those of biomolecules. Nanoparticles exhibit unique electronic, photonic and catalytic properties. The integration of nanoparticles with biomaterials displays unique recognition, catalytic, and inhibition properties, yield novel hybrid nano bio materials of synergetic properties and functions. The importance of functionalized nanoparticles for bio-medical applications cannot be overestimated. There has been reported some work about biological model system that various nanoparticles are applied as targeted biomarkers and drug-delivery agents and medical treatment. Especially silver nanoparticle have been reported as antimicrobial properties and are used as drugs. On the basis of these backgrounds, it occured to us that silver nanoparticles can be entrapped in nano-sized realm of DPPC bilayer, and it might affect the membrane fluidity at particular temperature(phase transition temperature)[30]. In our studies, silver-loaded liposome was prepared and fluidity of the DPPC bilayer containing silver nanoparticles was measured by ^{31}P NMR.

4.2 Previous MD and Other Experimental Studies

An experimental study by Verma and co-workers[31] shows that the internalization mechanism of spherical nanoparticles in the fibroblast cells strongly depend on the distribution of hydrophobic and hydrophilic domains on the surface of the nanoparticles. They observed that uniformly polar nanoparticles can be internalized by the

cell via an endocytotic pathway only. On the contrary, nanoparticles with the surface featuring ordered hydrophobic and hydrophilic stripes were able to translocate through the cell membrane via some direct mechanism, independent of endocytosis. Interaction of fully hydrophobic silver nanoparticles with dipalmitoylphosphatidylcholine(DPPC) lipid bilayer were explored by Bothun[2]. It was shown that hydrophobic nanoparticles tend to accumulate inside lipid bilayers and if present in sufficient concentration(more than 15:1 w/w DPPC/nanoparticle ratios), leads to a lowered melting temperature of the gel phase. In another example, single component phosphocholine bilayers in the presence of charged nano-particles have been investigated by Wang and co-workers[32]. Their results suggest that charged nanoparticlesposition themselves at the bilayer-water interface with negatively charged nanoparticlesincluding local gelation in the fluid bilayers, whereas positively charged nanoparticles cause local fluidization(disordering) in the gel phase. The effect of nanoparticle size on the stability of lipid membranes was investigated by Roiter et al.[33], using AFM measurements. It was shown that silica nanoparticles in a particular size range(between 1.2 nm and 22 nm) can cause formation of holes and defects in dimyristoylphosphatidylcholine(DMPC) bilayers. These are only a few examples of the recent studies of membrane-nanoparticles phenomena, varying broadly in the type of systems and nanoparticles under investigation, condition, methods, and observation. It is clear that systematic nanoparticle design requires a general fundamental framework within which membrane-nanoparticle systems can be described on a molecular level, disparate experimental observation explained and rationalized, and predictions on nanoparticle behavior as a function of its morphology made.

4.3 Various Models of NP-DPPC interactions

Several theoretical models of colloidal and nanoparticle interactions with lipid membrane have been proposed over the years, including those based on the Helfrich Hamiltonian and mean field theories.[34–40] However, these models often omit important

finer details on the structure of membrane, solvent, and other properties. Alternatively, coarse-grained(CG) models have recently been playing an increasingly important role in the studies of biological membranes.[39, 41] In these models, several atoms are represented as a single interaction site, and both implicit and explicit solvent models have been developed. The models have been applied to investigate the behavior of single and multicomponent lipid bilayers, vesicles, and micelles, as well as interaction of these entities with other species such as cholesterol, peptides, and proteins.[3]

Ramalho et. al[3] has employed molecular modeling to understand the structure of lipid bilayers and pathways of gel formation in the presence of nanoparticles. In this preliminary work they have concentrated on two specific cases reflecting recent experimental studies: a hydrophobic nanoparticle embedded in the core of a lipid bilayer and a charged nanoparticle at the surface of the bilayer. To investigate these phenomena on molecular level, they adopted a coarse grained forcefield developed by Marrink and co-worker[41] that has been employed to investigate the kinetics of fluid-gel phase transformations and, at the same time, has been also recently applied to study of the DPPC bilayer in the presence of several type of nanoparticles. In this study they have focused on the impact of different type of nanoparticles on the fluid-gel transformation rather than attempt to identify the location of the true phase coexistence. [3]

Several general concepts associated with fluid-gel phenomena in lipid bilayers and key observations have emerged from the studies of fluid-gel transformation by Marrink and co-workers[41] using an earlier version of MARTINI forcefield and single component DPPC bilayer as an exemplary and most characterized system. The most physiological relevent phase of a lipid bilayer is the disordered fluid phase L_α. Upon cooling, this phase undergoes a phase transition to a gel phase L_β, characterized, among several other available properties, by an ordered (but not crystalline) structure, substantially lower area per lipid compare to the fluid phase, and at the same time still substantial lateral mobility of the lipid compared to the proper crystalline phase. Several variants of the gel phase L_β have been observed with either perpendicular average orientation

of the lipid molecules to the plane of the bilayer(L_β) or oriented at a tilt angle ($L_{\beta'}$). For DPPC, the fluid-gel transition temperature is 315K. In reality, the actual temperature at which transformation from fluid to gel phase takes place may deviate from the equilibrium phase transition temperature towards lower values. The phase transformation from fluid to gel and from gel to fluid exhibits temperature hysteresis, which is a non-equilibrium, kinetically controlled phenomenon. Ramalho et. al[3] also briefly explored the effect of the nanoparticle presence on fluid-gel transformation from a kinetic perspective. They have shown that the rate of gel-phase growth is higher for the bulk lipid bilayer case, compared to that in the presence of nanoparticles. This effect is rather small for 3 nm hydrophobic nanoparticle or 6 nm positively charged nanoparticle, but it is more pronounced for the negatively charged nanoparticle at the bilayer surface. They have summarized the behavior of the lipid bilayer by studying the temperature dependence of surface area per lipid molecule. The presence of a hydrophobic nanoparticle or a positively charged nanoparticle at the bilayer surface does not significantly impact the fluid-gel transformation and it takes place at 288 K, the same temperature as for the bulk bilayer case. The presence of a negatively charged hydrophobic nanoparticle at the surface of the bilayer, however, delays formation of the gel phase, shifting of the location of the fluid-gel transformation to a lower temperature of 284K. This is consistent with the slow growth of gel phase in the presence of negatively charged nanoparticles. [3, 8]

Here we will see the change in the phase behavior of DPPC upon insertion of AgNP through ^{31}P NMR with varying temperature from 283K to 318K in steps of 5K. We recorded the changes in T_1, T_2 & Diffusion Coefficient with temperature.

4.4 Materials & Methods

DPPC, Chloroform and Ag-decanethiol nanoparticles(AgNPs) were obtained from Sigma-Aldrich. An average nanoparticle diameter was 3-10nm. Lipid assemblies were

prepared in Phosphate Buffered Saline(PBS) at 80 mM DPPC using the Bangham method[42]. AgNP concentration was fixed to provide DPPC/AgNP ratio 2:1(w/w) respectively. To form lipid/nanoparticle assemblies(LNAs), an aliquot of Ag-decanethiol NP/hexane solution was added to DPPC dissolved in chloroform to yield a transparent, miscible brown phase. The solvent phase was evaporated under nitrogen and the sample was placed under vaccum for 2 hours, leaving a dry DPPC/AgNP film. Hydration and processing steps were performed at 50°C, which is above the DPPC gel-fluid melting temperature(T_m=42°C). The film were hydrated with PBS, incubated for 1 hours, and sonicated for 2 hours.

4.5 Results & analysis

Experiments performed on a sample of DPPC bilayer in PBS buffer and with DPPC bilayer interacting with silver nanoparticles residing on Decanethiol. One dimensional proton experiment with water suppression is acquired for locating the regions in which the NMR signals corresponding to various components fall. Two dimensional homonuclear experiments : COSY, TOCSY and NOESY have also been performed to draw the H-H correlations in both sample types.

4.5.1 1D & 2D Proton Spectra

Protons in DPPC fall in the region of 0.5-1.5ppm as can be seen from Figure(4.1). On adding AgNP(Silver nanoparticle) with decanethiol as substrate, some of the proton signals from decanethiol overlap with that from DPPC, there can be seen some extra signals also in the range of 2-4ppm. We can see the similar pattern in NOESY spectra Figure(4.2) of extra signal in DPPC+AgNP with respect of DPPC alone. In case of COSY spectrum Figure 4.3(a) there can be seen correlation between two broad peaks of DPPC depicting direct coupling, while in Figure 4.3(b) two rectangles are made

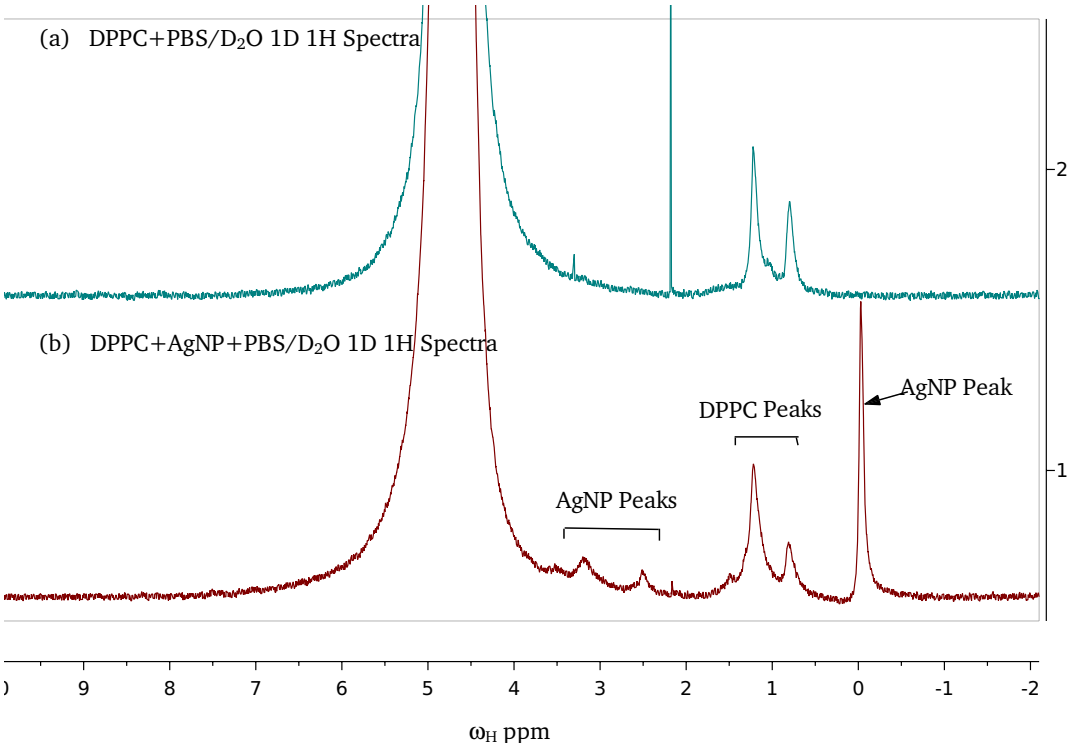

FIGURE 4.1: 1H spectra of DPPC & DPPC+AgNP

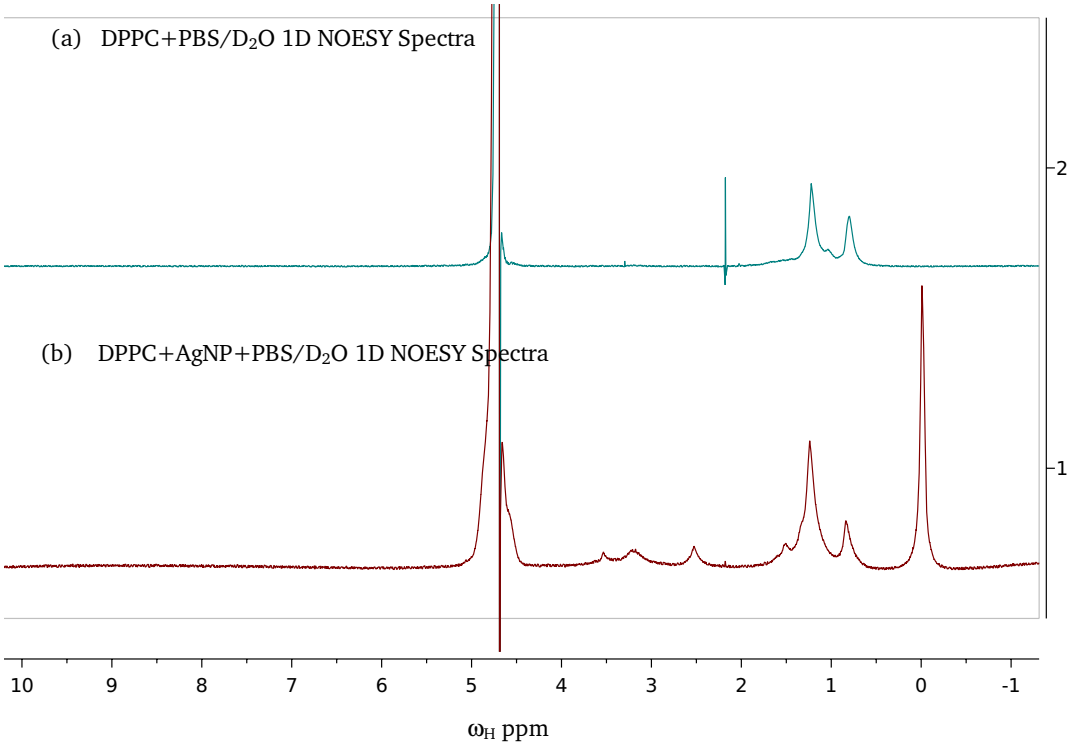

FIGURE 4.2: 1D NOESY Spectra of DPPC & DPPC+AgNP

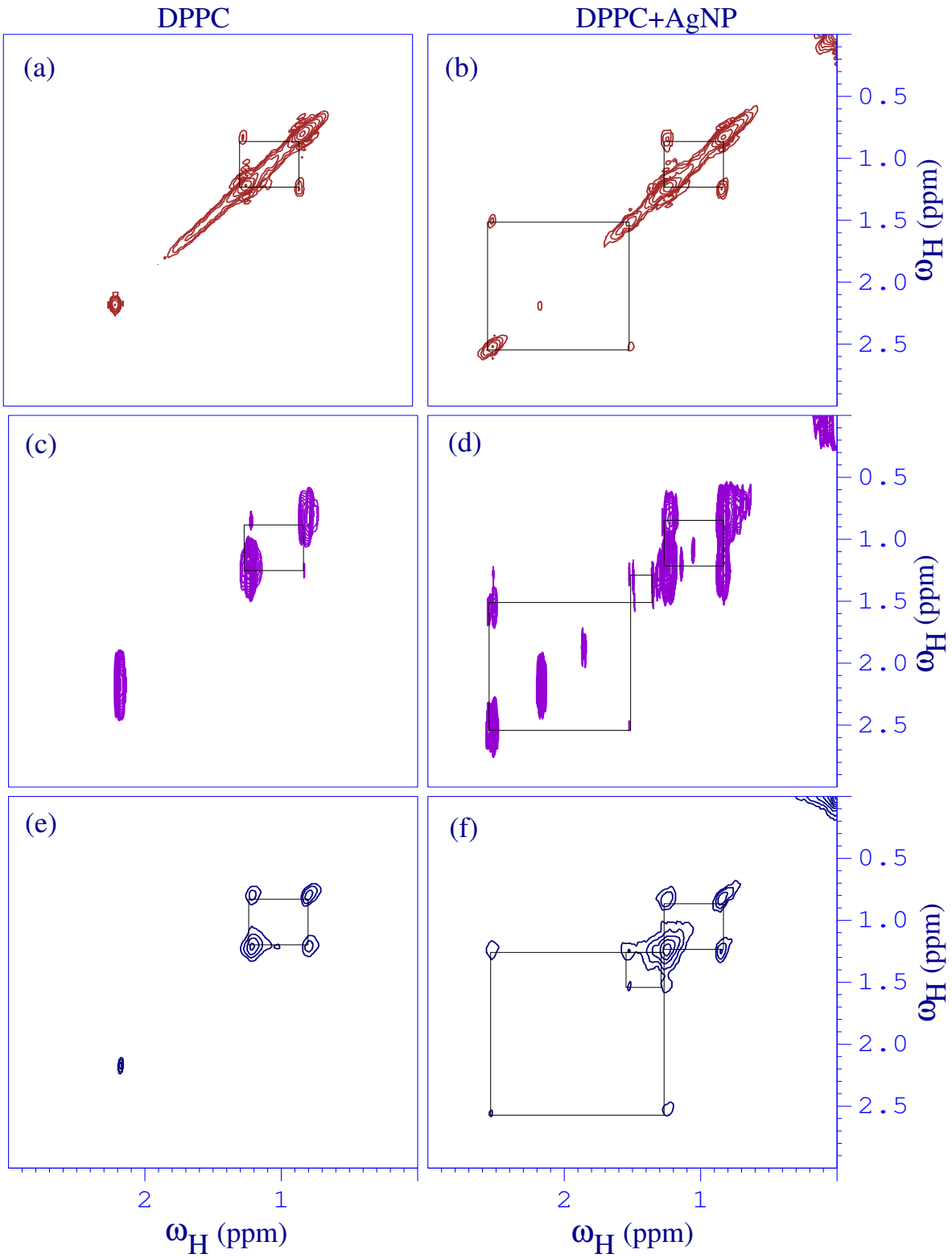

FIGURE 4.3: (a),(b) contains the COSY spectrum , (c),(d) contains TOCSY and (e),(f) bear NOESY spectrum for DPPC and AgNP+DPPC respectively. Related crosspeaks are joined in all the spectra types showing the proton-proton correlations.

showing two correlations : one among the protons in DPPC which is same as in case of DPPC alone and one corresponding to decanethiol among the peak at 2.53ppm and the peak near the foot of the DPPC signal. Performing TOCSY is not introducing any new correlations in the DPPC sample but one faint pair of crosspeaks is seen corresponding to peaks at 1.49ppm and 1.34ppm in AgNP+DPPC. Thus the protons at 1.5 ppm are coupled to protons at 1.34 ppm and at 2.53 ppm. All these possibly belong to decanethiol. Things become interesting when we come across NOESY spectrum which reflects the homonuclear correlations through space. There exist only one correlation in case of DPPC alone which is expected. Close look at the NOESY spectrum of DPPC+AgNP, shows three pairs of crosspeaks (joined by rectangles) peak at 1.34ppm is spatially correlated to signal embedded in the broad peak centered around 1.26ppm. Signal at 1.34ppm is from Decanethiol but the one at 1.26ppm is coming from both DPPC as well as Decanethiol. This particular correlation is not found in the COSY spectrum and hence witnesses the spatial disturbances which is arising from interaction of silver nanoparticles with DPPC bilayer.

Experimental parameters: Three homonuclear correlation experiments are performed - cosyqf using gradients, phase sensitive NOESY using gradients with mixing time of 500ms and TOCSY with Hartman-Hahn transfer using mlev17 sequence taking mixing time of 60ms. Spectral width of 12ppm in both the dimensions are acquired for COSY, NOESY experiments and 10ppm in case of TOCSY. In all the experiments, 16 transients are collected. Sined gradient pulse is applied with strength 40% in NOESY and 10% in COSY. For 1D ^{31}P experiments Spectral Width(SW) is taken as 395 ppm with transmitter frequency offset(o1p) as -50ppm. Inter-scan delay is 5 Seconds & transients 16 in all 1D ^{31}P experiments.

4.5.2 ^{31}P Experiments

All the ^{31}P experiments are performed at Avance III 400MHz spectrometer equipped with BBO probe. Being equipped with the two systems one containing DPPC bilayer

TABLE 4.1: Spin lattice relaxation time T_1 of ^{31}P in DPPC and AgNP+DPPC at different temperatures.

S.No.	Temperature (in Celcius)	T_1 (s) (for DPPC)	T_1 (s) (for DPPC+AgNP)
(1)	10	2.9673	2.6300
(2)	15	2.9578	2.7036
(3)	20	2.9029	2.6507
(4)	25	2.6066	2.3376
(5)	30	2.5865	2.4366
(6)	35	2.7928	2.7100
(7)	40	2.7271	2.7117
(8)	45	2.7787	2.7107

TABLE 4.2: Spin-spin relaxation time T_2 of ^{31}P in DPPC and AgNP+DPPC at different temperatures.

S.No.	Temperature (in Celcius)	T_2 (s) (for DPPC)	T_2 (s) (for DPPC+AgNP)
(1)	10	0.1798	0.0518
(2)	15	0.1741	0.0494
(3)	20	0.1498	0.1304
(4)	25	0.2591	0.0916
(5)	30	0.2151	0.0699
(6)	35	0.1007	0.0387
(7)	40	0.0801	0.0346
(8)	45	0.0612	0.0310

and one with the interacting AgNPs (as clear from the 2d spectra analysis), we proceed towards studying dynamics. As we know that phosphorous(^{31}P) is NMR active and in the system under study, only DPPC contains phosphorous. Thus ^{31}P can act as our marker, making the dynamical study precise and the distinctions in observations clear. We are starting with the lyposomal structure of lipid bilayer with silver nanoparticles embedded in it. [43]

TABLE 4.3: Diffusion coefficients for DPPC and AgNP+DPPC using ^{31}P NMR at different temperatures.

S.No.	Temperature (in Celcius)	Diffusion Coefficient(in m^2s^{-1}) (for DPPC)	(for DPPC+AgNP)
(1)	10	1.5864×10^{-10}	1.3810×10^{-10}
(2)	15	1.8664×10^{-10}	1.6151×10^{-10}
(3)	20	2.1589×10^{-10}	1.8408×10^{-10}
(4)	25	2.6368×10^{-10}	2.0319×10^{-10}
(5)	30	3.0946×10^{-10}	2.7654×10^{-10}
(6)	35	3.7312×10^{-10}	2.7153×10^{-10}
(7)	40	10.5052×10^{-10}	2.7838×10^{-10}
(8)	45	12.8880×10^{-10}	4.0186×10^{-10}

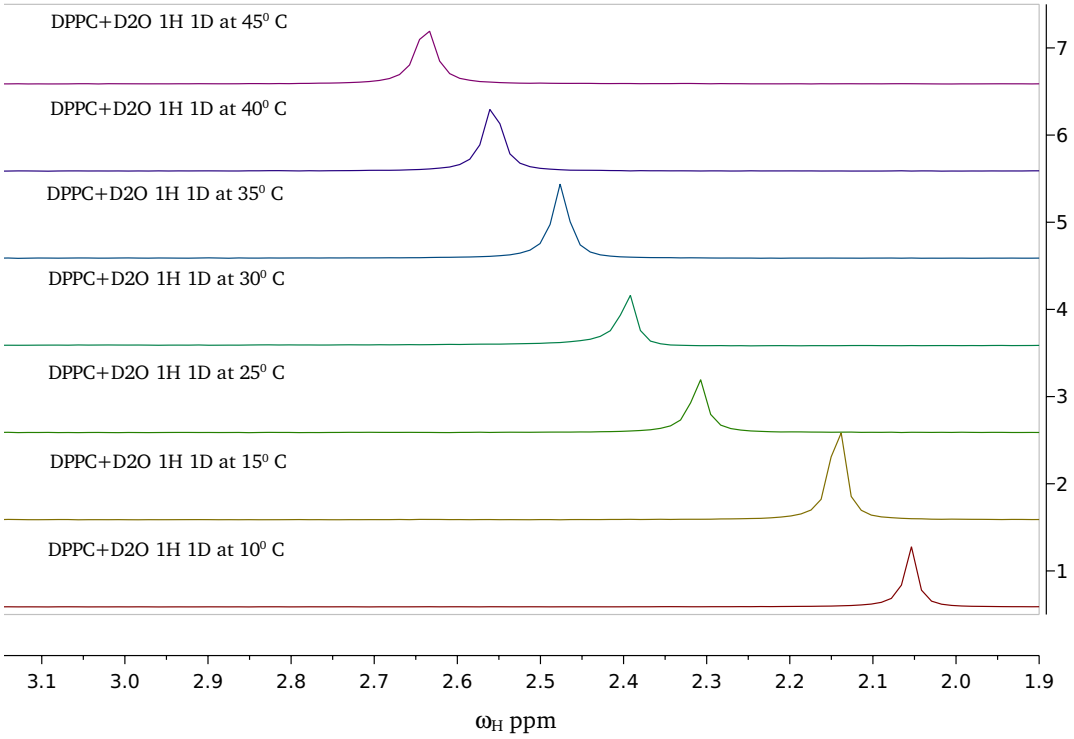

FIGURE 4.4: Shifting of 31P signals of DPPC on Different Temperature(on actual scale)

DPPC in Lipid bilayer form transits from Gel phase to liquid in the temperature ranging from $10-40^0$C. ^{31}P NMR Experiments are performed at different temperatures. The NMR signal gradually shifts towards higher ppm values with temperature increasing from 10^0C to 40^0C (fig 4.4 & 4.5). Spin lattice relaxation time(T_1) for ^{31}P

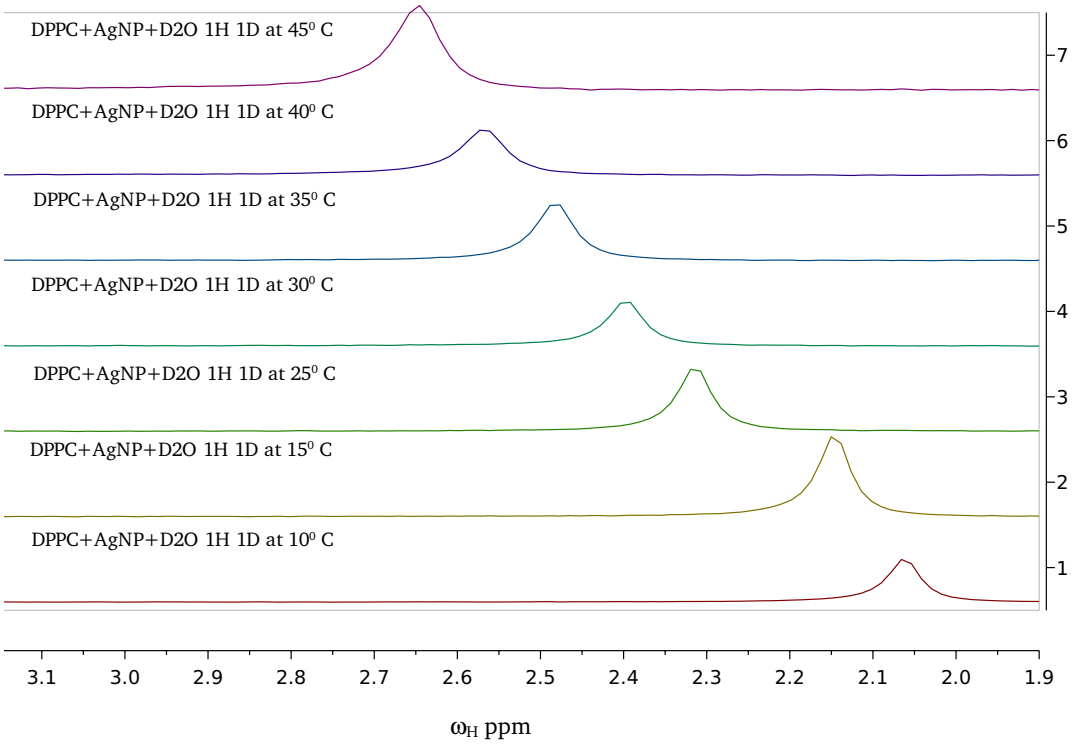

FIGURE 4.5: Shifting of 31P signal of DPPC+AgNP with Varying Temperature(on actual scale)

in both the systems is found at regular temperature intervals shown in table(4.1) and the fig(4.6). The plot clearly shows the faster build up of longitudinal magnetization during the phase transition in both cases. This happens due to the presence of inhomogeneous mixture of liquid and gel phase at the same time. Also T_1 corresponding to AgNP+DPPC is lower than that of DPPC alone at the corresponding temperatures, which is expected. [44]

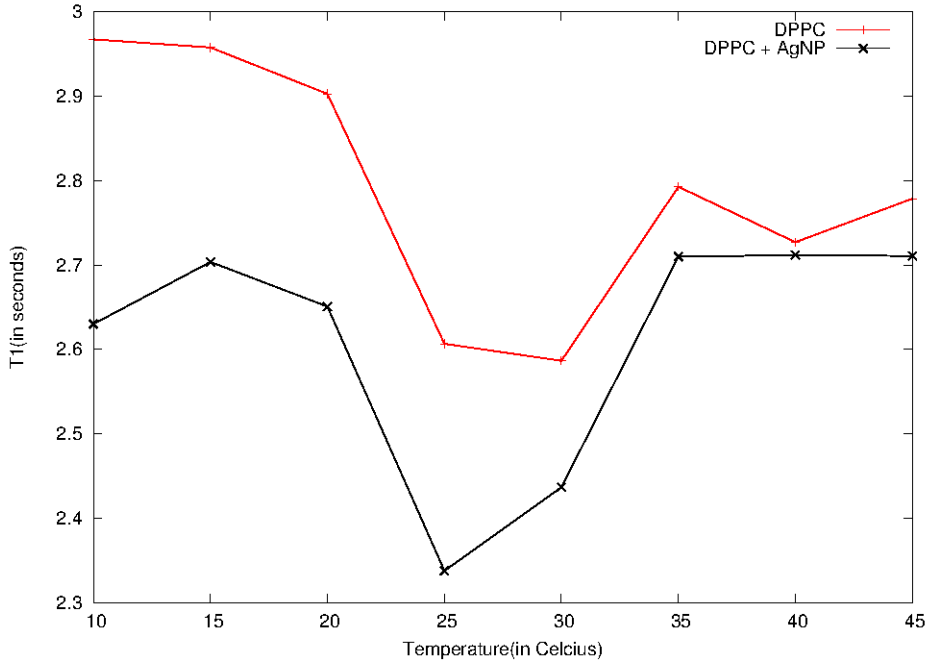

FIGURE 4.6: DPPC and AgNP+DPPC T1 Relaxation plot with varying temperature

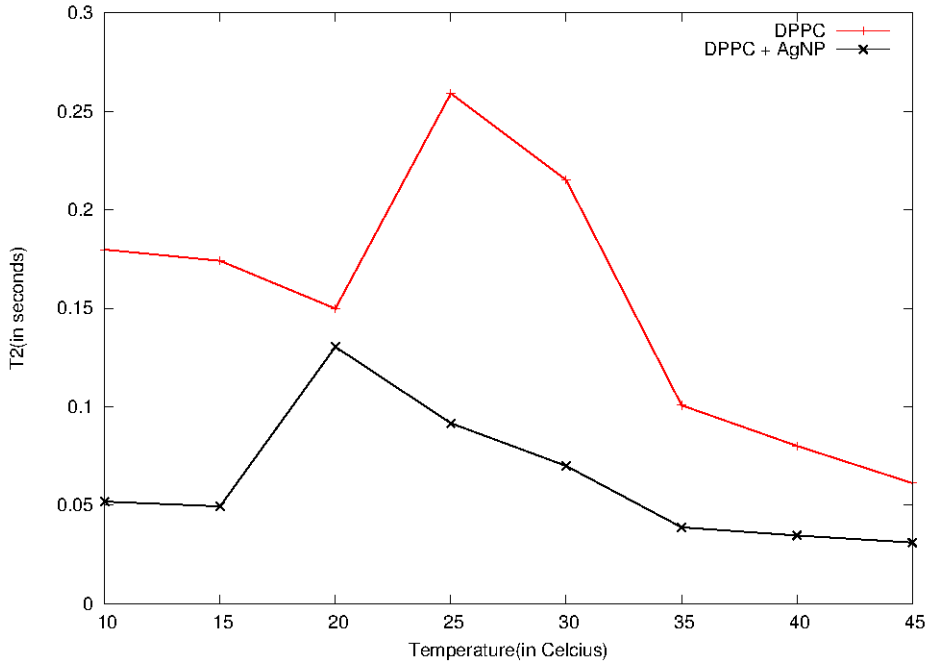

FIGURE 4.7: DPPC and AgNP+DPPC T2 Relaxation plot with varying temperature

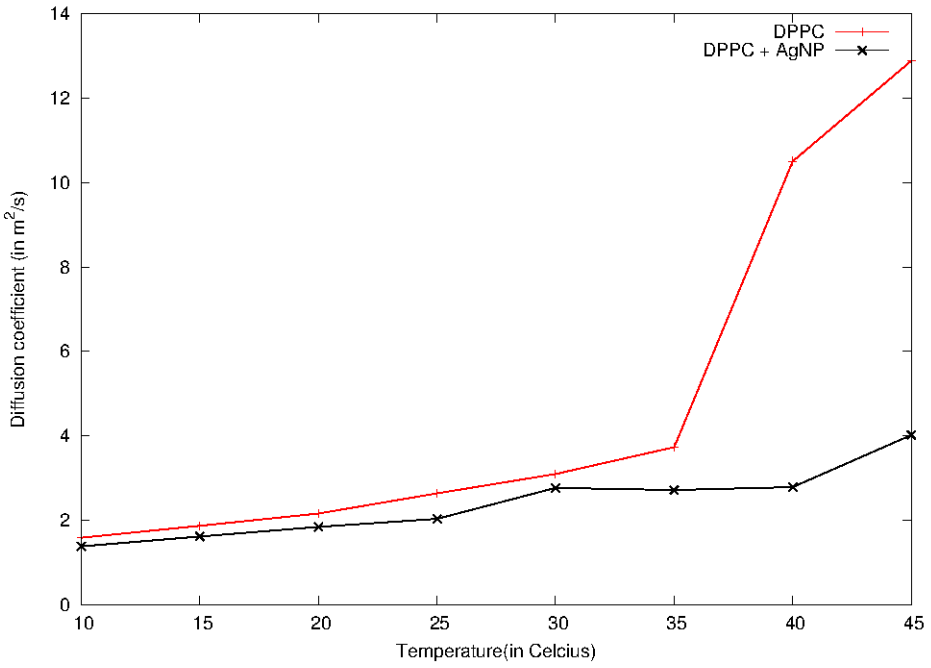

FIGURE 4.8: DPPC and AgNP+DPPC diffusion coefficient plot with varying temperature. After 35 degree Celsius diffusion coefficient of DPPC becomes significantly higher compare to DPPC+AgNP which suggests that Phase transition occur in DPPC after that temperature. It get converted from gel phase to fluid phase and that result in higher diffusion coefficient. On the other hand DPPC+AgNP does not show such behavior even on higher Temperature.

T_2 relaxation studies(table(4.2), fig(4.7)) also show lower values of relaxation time and hence faster relaxation in case of AgNP+DPPC than in DPPC. Abrupt behavior is observed in the temperature range $15-35^0$C. Diffusion studies are highly temperature dependent. Diffusion coefficient for phosphorous is found at different temperatures as shown in table. As can be seen from table(4.3) and fig(4.8), rate of diffusion increases with increasing temperature. Under the effect of gradients of varied strengths, the whole liposomal structure diffuses and we can get an average rate of diffusion of DPPC bilayer. Addition of AgNPs bring in distortions in the system making it more bulky and hence diffuses relatively slow. The plot in Figure(4.8) shows lower value of diffusion coefficient in case of AgNP+DPPC than that of DPPC alone at corresponding values of temperature. In other words, due to embedded AgNP, there exist higher values of hydrodynamic radii in case of AgNP+DPPC which is inversely proportional

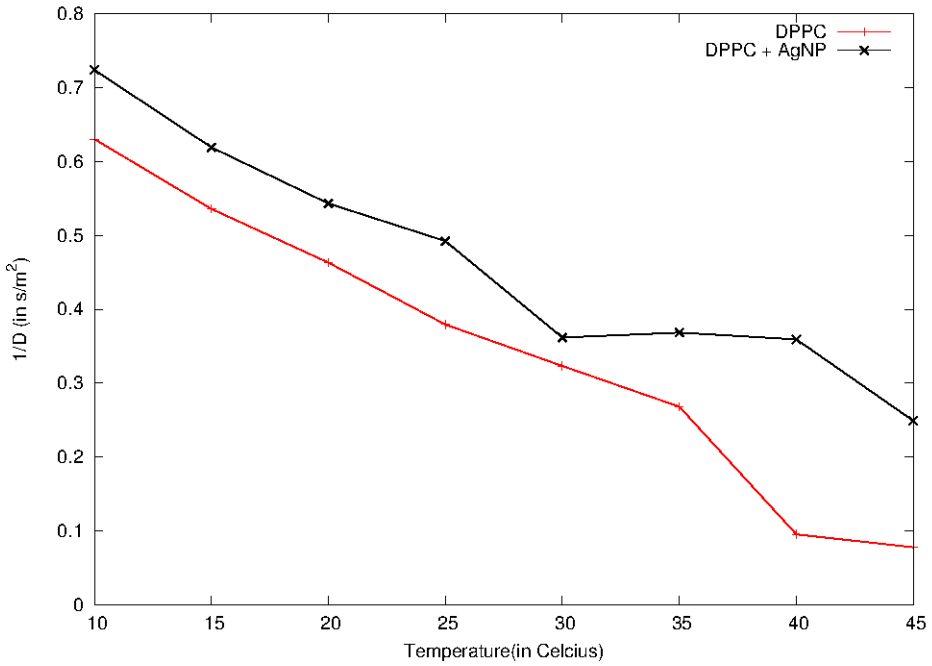

FIGURE 4.9: DPPC and AgNP+DPPC 1/D(hydrodynamic radius) plot with varying temperature

to the diffusion coefficient. Dependence of inverse diffusion coefficient on temperature is shown in Figure(4.9).

Chapter 5

AgNP Diffusing in Polymer Mesh

5.1 Introduction

Understanding the transport properties of nano- and micrometer sized particles in crowded solutions of macromolecules is important in various problems of medical and technological interests, such as chromatography, electrophoresis, and drug delivery. In the field of biophysics, the modeling of cellular processes, such as enzymereactions, critically rely on understanding the diffusion of globular proteins in crowded cytoplasmic environments.[45, 46] In the area of polymer physics, the dynamics of particles can provide important information about the local mechanical and viscoelastic properties of the solution, an approach widely used in microrheology.[47, 48] A large body of experimental work has focused on comparing the experimentally measured translational diffusion coefficient (D) of the particles with the prediction from Stokes-Einstein(SE) relation using the known polymer macroscopic viscosity(η).[49, 50] Though there are some discrepancies, the results generally indicate that when the size of the particle (R) is much greater than the correlation length(ξ) of the polymer solution, the medium behaves as a continuum fluid. In this scenario, the mobility of the particle is coupled to the chain relaxation; hence, the particle experiences the macroscopic zero shear

rate viscosity and the particle diffusion satisfies the SE relation. In the opposite case when $R \ll \xi$, the particles generally experience the local microscopic viscosity, which is a strong function of the length scale at which it is probed. The local viscosity is generally lower than the microscopic viscosity of the polymer solution, therefore in this situation the particle mobility is faster compared to SE prediction [21, 51]. Small proteins and nano-particles diffuse surprisingly quickly in living cells and in other high viscosity complex liquids. Their diffusion coefficients are often orders of magnitude larger than expected from the Stokes-Sutherland-Einstein(SSE) relation and solution macroscopic viscosity, η_{macro}[52]. Here we will focus on the diffusion of Silver Nanoparticle in Triblock Copolymer(PEG-PPG-PEG) in different solvent like D-Benzene and D_20.

Polymeric Vesicles: polymeric vesicles were first investigated as a means of stabilizing the metastable self assemblies formed from low molecular weight amphiphiles, with the polymer providing a kinetic trap for the self assembled system. A wealth of polymer architectures are now known to assemble into vesicles: namely block copolymer, random graft copolymer, polymerized self assembling monomers and polymers bearing lipid pedant groups. Additionally, polymeric vesicles, although not normally termed as such, arise from the self assembly of amphiphilic polymers, i.e. poly(oxyethylene) amphiphiles with: (a) lipids to give poly(oxyethylene) coated liposomes, or (b) non-ionic surfactants to give poly(oxyethylene) coated niosomes. [19]

Block copolymer vesicles, termed 'polymersomes' are fairly new discoveries, being first reported in the 1990s. Polymersomes have been prepared from a variety of block copolymers. There is a clear relationship between the hydrophobic content of polymers and self assembly. Vesicle sizes are varied and range from tens of nanometers to tens of microns. The thickness of the membrane is determined by the degree of polymerization in the hydrophobic block and these extra thick membranes confer, on the vesicle, exceptional stability to soluble surfactants and mechanical stress.[19]

5.2 Physics of Polymer Network & meshes

Multicomponent solutions consisting of polymers, surfactants, proteins, and other macromolecules are common to many biological systems as well as cosmetic and pharmaceutical preparations. The understanding of the nature of macromolecular aggregates and complexes is consequently of great technological relevance. [51] NMR spectroscopy has been used as a powerful technique to study macromolecular dynamics in these systems, since it can report on molecular motion inside the aqueous solutions via the longitudinal relaxation time T_1 and the transverse relaxation time T_2. In addition, pulsed-field-gradient diffusion NMR spectroscopy is used to measure the molecular self-diffusion coefficient. All of these physical quantities will change due to the interaction between molecules, molecular aggregation, and micellization.[53]

Polyethylene oxide(PEO) and polyethylene glycol(PEG) are polymers with the subunit C-O-C. They are well-known encapsulating agents for drug delivery,[54] solvents for low temperature crystallography,[55] and modulators of osmotic pressure.[56] Low molecular weight PEG readily passes through the pores of membrane proteins,[57] and in fact, can be sized by single channels.[58] Comparisons with crystal structures and electron micrographs indicate that the pore radius, R_p, is close to the effective hydrodynamic radius in the solution, R_h, of the largest PEG able to diffuse through the pore or to block ion conductance. [59]

Self-assembly on the mesoscopic length scale tends to impose severe internal constraints on molecular diffusion. These constraints act as *internal restrictions* on molecular propagation, analogously to the external *confinement* characteristic of typical host-guest systems. Specific symmetry and connectivity properties of local molecular ordering tend to inhibit three-dimensional isotropy. Block Copolymer(BCP) exhibit a rich variety of equilibrium symmetries(spherical, cylindrical and lamellar) which can be controlled by varying concentration, temperature, and block composition. [60, 61]

5.3 Materials & Methods

Triblock Copolymer(PEG-PPG-PEG) with M_n as 1100 was purchased from Sigma-Aldrich. Silver Nanoparticle substrated on Decanethiol dispersed in Hexane was also purchased from Sigma-Aldrich. Four type of samples were made: 1) 10% Triblock Colpoymer(PEG-PPG-PEG) in D-Benzene 2) 10% Triblock Copolymer(PEG-PPG-PEG) in D_2O and 3) 10% Triblock Copolymer(PEG-PPG-PEG) in AgNP + D-Benzene 4) AgNP in D-Benzene. Sodium Dodecyl Sulphate(SDS) was also purchased from Sigma Aldrich. All samples were made on Room Temperature.

Experimental Parameters: Homonuclear correlation experiment COSY is performed-cosygpqf using gradients with inter-scan delay(D1) as 1 second. Time domain(td) for both axis was respectively 1028 & 128. Transmitter frequency offset(o1p) was 5 ppm & Spectral width was 10 ppm in both dimensions for all experiments performed. 64 transients are collected. Sined gradient pulse is applied with strength 10% in COSY. 1D experiments were performed with 16 transients and D1 as 2 second.

5.4 Results & Analysis

Triblock Copolymer(PEG-PPG-PEG) sample was dissolved in D_2O and after that one dimensional proton, carbon spectra and two dimensional COSY Spectra was recorded. Then Triblock Copolymer(PEG-PPG-PEG) was mixed in D-Benzene because of its compatibility with Silver Nanoparticle. Silver Nanoparticles were added in Triblock Copolymer(PEG-PPG-PEG) & D-Benzene mixture. 1D proton, carbon, 2D COSY spectras were then recorded for the same. The same process was repeated for Sodium Dodecyl Sulphate(SDS) too (figure 5.3).

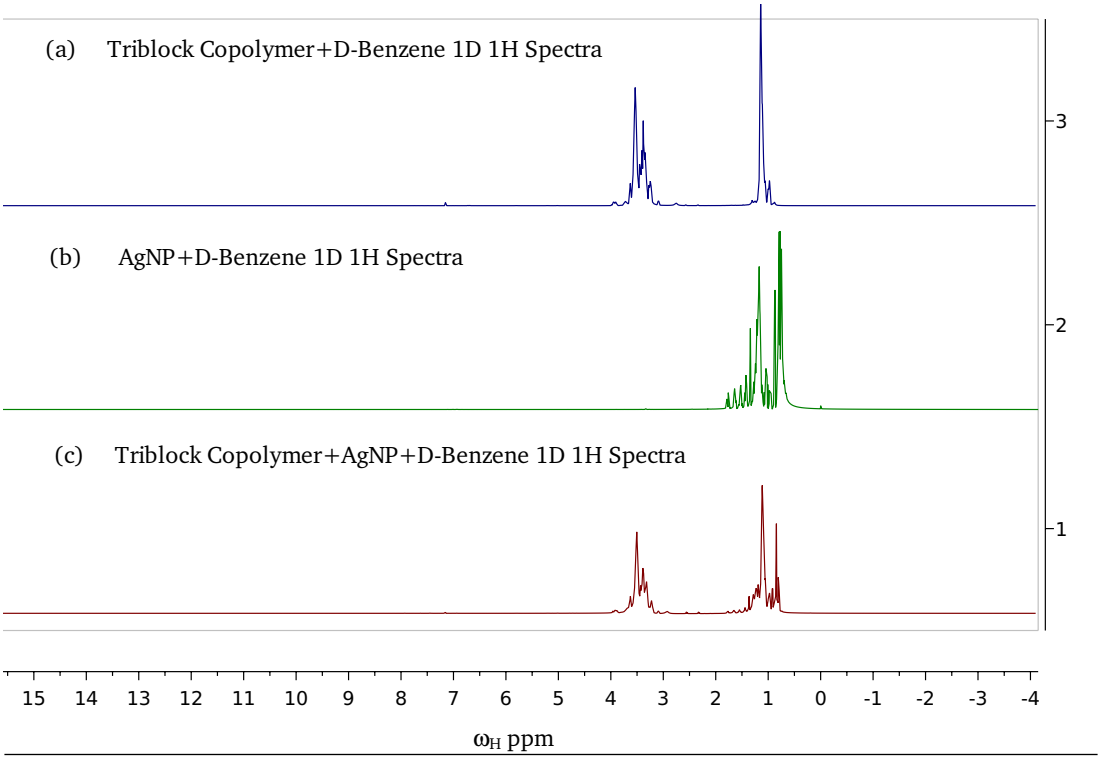

FIGURE 5.1: Effect of AgNP upon 1H spectra of Triblock Copolymer

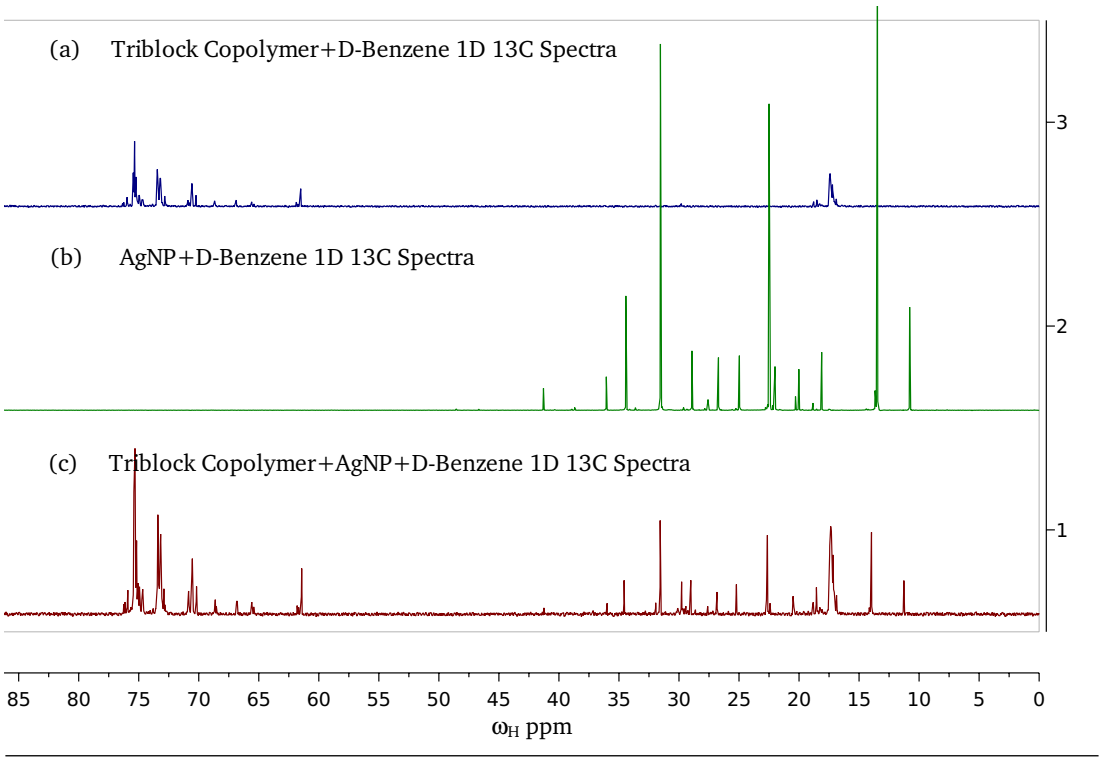

FIGURE 5.2: Effect of AgNP upon 13C spectra of Triblock Copolymer

Protons in Triblock Copolymer fall in the region around (0.85-1.30 ppm) & (3.0-4.0 ppm) as shown in fig 5.1. Silver Nanoparticle alone has a proton frequency rage from (0.5-1.8 ppm). If we add AgNP to Triblock Copolymer(PEG-PPG-PEG) then some proton spectra overlap with Triblock Copolymer(PEG-PPG-PEG). Similar case was with carbon spectra(figure 5.2) as Triblock Copolymer has range (17-19 ppm & 61-77 ppm), but AgNP has range from (10-42 ppm) so there is a overlap region from (17-19 ppm), other than that spectral peaks are in different regions. Now if we see the COSY spectra, some new correlations come up due to AgNP. We can compare Figures 5.4, 5.5 & 3.5. We see that if the COSY Spectra of AgNP alone is observed then there are no correlation peaks around (3.90 ppm & 3.95 ppm). Triblock Copolymer alone gives correlation peaks around (3.90 ppm & 3.95 ppm) but the mixture of these have some shifting in the correlation peaks that suggests that AgNP are binding to Triblock Copolymer at some site.

In case of SDS it happens in reverse way. Some correlations which were coming in

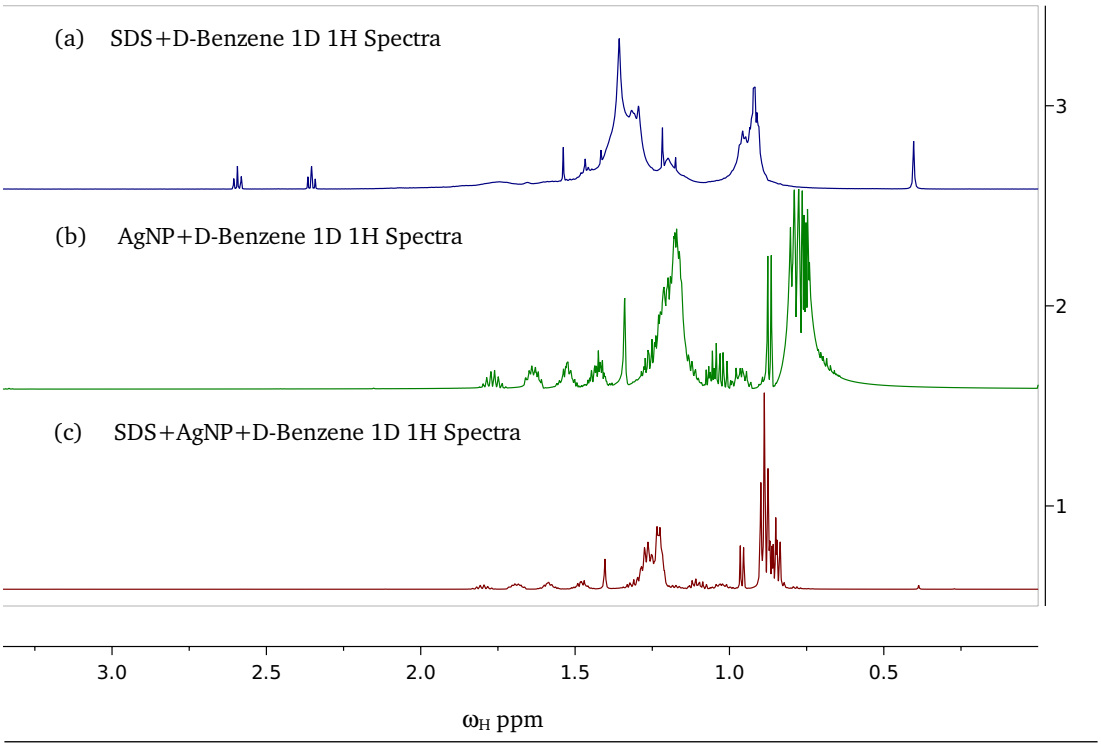

FIGURE 5.3: (a) 1D 1H Spectra of Sodium dodecyl Sulphate(SDS) in D-Benzene solvent. Spectra has some extra peaks at above 2.25 ppm which are totally absent in the mixture of SDS & AgNP. (b) Silver Nano particle 1D-1H Spectra (c) SDS+AgNP Spectra has some peaks due to AgNP but some SDS peaks are absent in this spectra and also there is some shifting in peaks too due to presence of AgNP inside SDS mesh

SDS alone 2D COSY Spectra(Figure 5.6) were absent in the mixture(Figure 5.7). That means presence of AgNP affects the correlations of SDS itself and disturb its dynamics too.

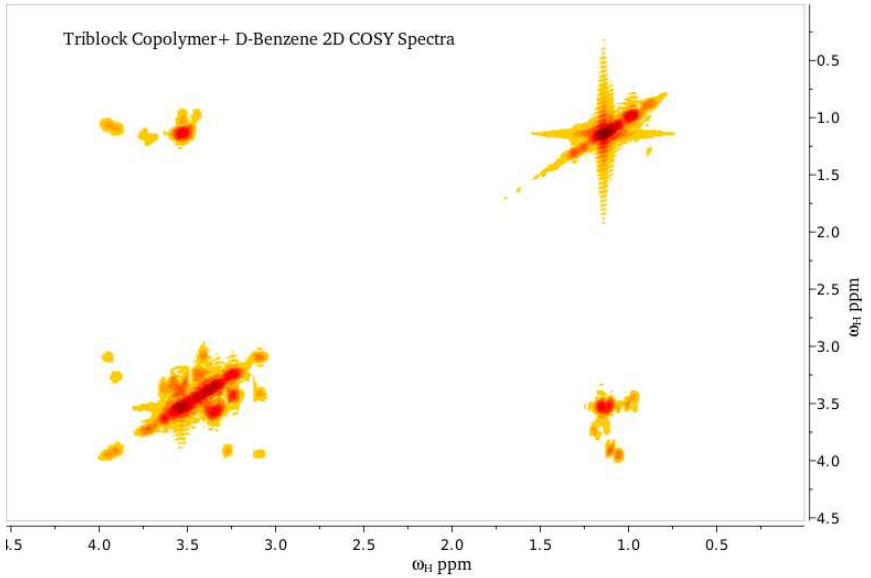

FIGURE 5.4: 2D COSY Spectra of Triblock Copolymer(PEG-PPG-PEG) + D-Benzene

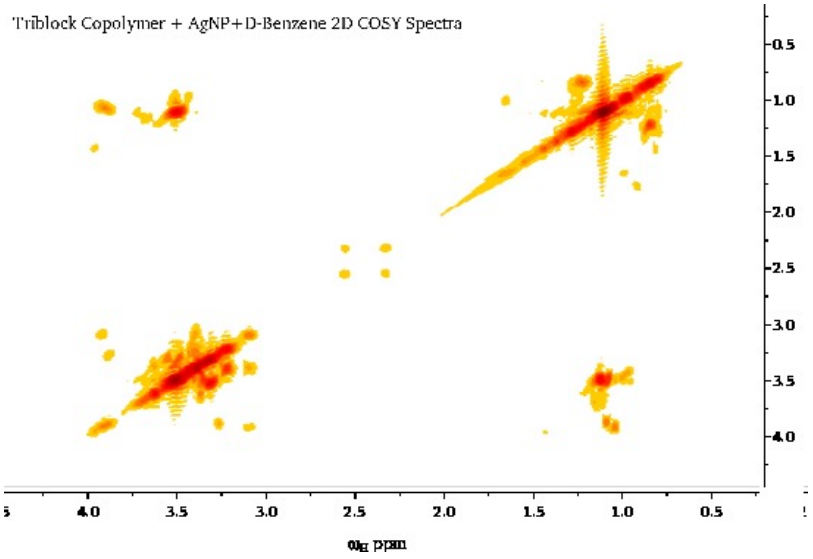

FIGURE 5.5: 2D COSY Spectra of Triblock Copolymer(PEG-PPG-PEG) + AgNP + D-Benzene

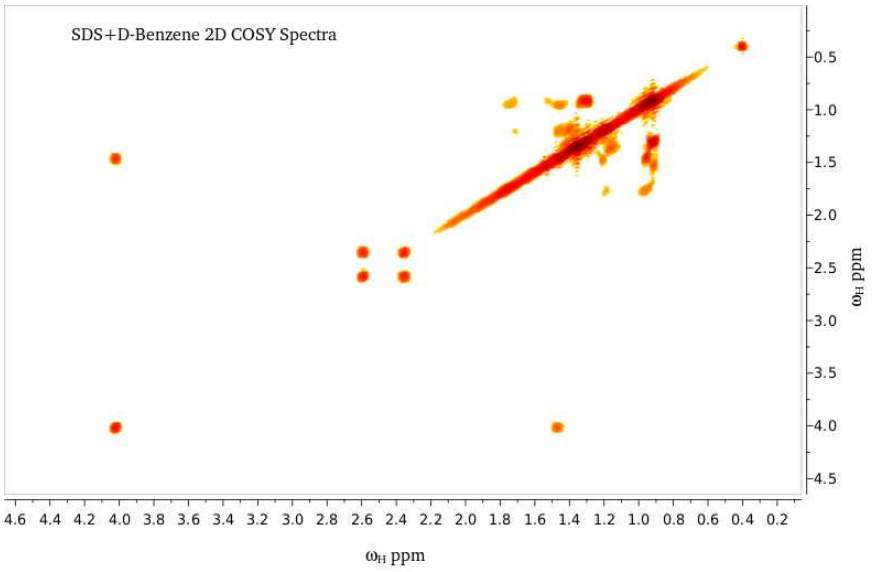

FIGURE 5.6: 2D COSY Spectra of Sodium Dodecyl Sulphate(SDS) + D-Benzene

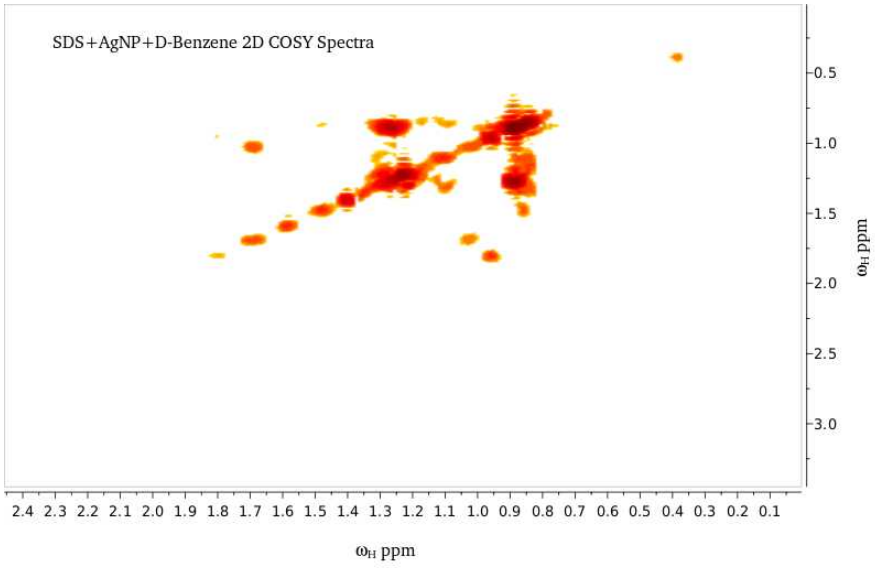

FIGURE 5.7: 2D COSY Spectra of Sodium Dodecyl Sulphate(SDS) + AgNP + D-Benzene

Chapter 6

Summary and Outlook

T_1 Relaxation, T_2 Relaxation & Diffusion experiments of ^{31}P performed on DPPC Lipid Bilayer in absence & presence of Silver Nanoparticles(AgNP) clearly show that the phase behavior of DPPC Bilayer changes drastically after introducing AgNP. Figures 4.6, 4.7, 4.8, and 4.9) depict that as temperature varies from 10°C to 40°C, DPPC Bilayer transforms from gel phase to liquid phase gradually. We can see from the Figures 4.6 and 4.7 that temperatures below 20°C contain pure gel phase of DPPC Bilayer and temperatures above 35°contain pure liquid phase of the same, however both the phases coexist in the range 20°to 35°. Some shifting of this transition zone has been seen after adding AgNP.

Triblock Copolymers(PEG-PPG-PEG) & sodium Dodecyl Sulphate(SDS) also show some different correlations if we compare 2D COSY Spectras of Triblock & SDS alone(Figures 5.4 and 5.6) and after adding AgNP (Figures 3.5, 5.5, and 5.7). Overlapping of some peaks of Triblock & AgNP in 1D spectras(Figures 5.3, 5.1, and 5.2) suggested that there can be some new correlations because of attachment of AgNP in the Triblock Copolymer Mesh. After performing 2D COSY spectra we indeed got some new correlations in the case of Triblock and some correlations are missing in the case of SDS. This confirms the effect of AgNP on the Mesh of Triblock or SDS.

We can crosscheck these results with the help of Molecular Dynamics(MD) Simulations or other experimental techniques. T_2 relaxation study with temperature in these systems are to be done in more detail because of its strange behavior in both DPPC & DPPC+AgNP. We can apply the same technique in some real systems like Actin and see the effect of Silver Nanoparticles on its diffusion and phase properties.

Appendix A

Fourier transform

The Fourier transformation defines a relationship between one function in the time domain and another function in the frequency domain:

$$S(\omega) = F\{s(t)\} = \int_{-\infty}^{\infty} s(t)e^{-i\omega t}dt; \tag{A.1}$$

$$S(\nu) = F\{s(t)\} = \int_{-\infty}^{\infty} s(t)e^{-i2\pi\nu t}dt, \tag{A.2}$$

in which $\omega = 2\pi\nu$. The two functions s(t) and $S(\omega)$[or s(t) and $S(\nu)$] are said to form a Fourier transform pair. The inverse Fourier transformations are defined by

$$s(t) = F^{-1}S(\omega) = \frac{1}{2\pi}\int_{-\infty}^{\infty} S(\omega)e^{i\omega t}d\omega; \tag{A.3}$$

$$s(t) = F^{-1}\{S(\nu)\} = \int_{-\infty}^{\infty} S(\nu)e^{i2\pi\nu t}d\nu, \tag{A.4}$$

Fourier transformation and inverse Fourier transformation are linear operations and satisfy the relationships.

$$F\{cs(t)\} = cF\{s(t)\}; \tag{A.5}$$

$$F\{s(t) + r(t)\} = F\{s(t)\} + F\{r(t)\}, \tag{A.6}$$

in which c is a complex constant.

For completeness, some important theorems concerning Fourier transformations are listed below; proofs of these theorems can be found in standard texts:[62]

1. Similarity:
$$F\{s(at)\} = \frac{1}{|a|}S(\omega/a) = \frac{1}{|a|}S(\nu/a). \tag{A.7}$$

2. Time Shifting:
$$F\{s(t-\pi)\} = e^{-i\omega\tau}S(\omega) = e^{-i2\pi\nu\tau}S(\nu). \tag{A.8}$$

3. Frequency Shifting:
$$F\{s(t)e^{-i\omega_0\tau}\} = S(\omega-\omega_0); \tag{A.9}$$
$$F\{s(t)e^{-i2\pi\nu_0\tau}\} = S(\nu-\nu_0). \tag{A.10}$$

4. Derivative theorem:
$$F\{\frac{d^k}{dt^k}s(t)\} = (i\omega)^k S(\omega) = (i2\pi\nu)^k S(\nu). \tag{A.11}$$

5. Convolution: If the *convolution integral* of two functions r(t) and s(t) is defined as
$$r(t) * s(t) = \int_{-\infty}^{\infty} r(\tau)s(t-\tau)d\tau, \tag{A.12}$$
then
$$F\{r(t) * s(t)\} = R(\omega)S(\omega) = R(\nu)S(\nu) \tag{A.13}$$

6. Correlation: If *correlation integral* of two functions r(t) and s(t) is defiend as
$$Corr[r(t), s(t)] = \int_{-\infty}^{\infty} r(t+\tau)s(\tau)d\tau, \tag{A.14}$$
then
$$F\{Corr[r(t), s(t)]\} = R(\omega)S^*(\omega) = R(\nu)S^*(\nu) \tag{A.15}$$

in which $S^*(\omega)$ and $S^*(\nu)$ are the complex conjugates of $S(\omega)$ and $S(\nu)$, respectively.

7. Parseval's theorem:

$$\int_{-\infty}^{\infty} |s(t)|^2 dt = \int_{-\infty}^{\infty} |S(\omega)|^2 d\omega = \int_{-\infty}^{\infty} |S(\nu)|^2 d\nu \tag{A.16}$$

These theorems have important practical consequances for NMR spectroscopy. The similarity theorem demonstrates that broadening of a function in one dimension results in narrowing of the function in other dimension. The time-shifting theorem demonstrates that delaying acquisition(intentionally or due to instrumental delay) in the time domain results in a frequancy-dependent phase shift in frequency domain. The frequency-shifting theorem permits the apparent frequencies in the frequency domain to be shifted after acquisition. The convolution and correlation theorems provide efficient means of calculating the convolution and correlation of two functions. In most cases, it is more efficient to Fourier-transform both functions, multiply their transforms, and inverse-Fourier-transform the result to obtain the convolution or correlation than by direct integration. As discussed later, apodization of the free induction decay in the time domain is performed to convolute the signal in the frequency domain with a more desirable lineshape function. Parseval?s theorem demonstrates that the signal energy is identical in the two domains and implies that the information content of the signal is identical in the time and frequency domains.[62]

The most important operation for pulsed Fourier transform NMR spectroscopy in liquids is the Fourier transform of the time-domain signal for a damped oscillator, which is given by

$$s(t) = I_0 \exp[(i\omega_0 - \lambda_0)(t + t_0) + i\phi_0] \tag{A.17}$$

for $t \geq 0; s(t) = 0$ for $t < 0$. I_0 is the initial signal amplitude, ω_0 is the frequency, λ_0 is the decay constant(usually the transverse relaxation rate constant), ϕ_0 is the initial signal phase, and t_0 is the value of the initial sampling delay. The initial sampling

delay may arise from instrumental delays or may be intentionally set. The Fourier transform of s(t) is

$$S(\omega) = I_0 \exp[(i\omega_0 - \lambda_0)(t_0) + i\phi_0] \int_0^\infty \exp\left[i(\omega_0 - \omega) - \lambda_0\right] t dt \tag{A.18}$$

$$= I_0 \exp[(i\omega_0 - \lambda_0)(t_0) + i\phi_0] \frac{\exp\left[i(\omega_0 - \omega) - \lambda_0\right] t}{i(\omega_0 - \omega) - \lambda_0} |_0^\infty \tag{A.19}$$

$$= I_0 \exp[(i\omega_0 - \lambda_0)(t_0) + i\phi_0] \frac{-1}{i(\omega_0 - \omega) - \lambda_0} \times \frac{-i(\omega_0 - \omega) - \lambda_0}{-i(\omega_0 - \omega) - \lambda_0} \tag{A.20}$$

$$= I_0 \exp[(i\omega_0 - \lambda_0)(t_0) + i\phi_0] \frac{i(\omega_0 - \omega) + \lambda_0}{(\omega_0 - \omega)^2 + \lambda_0^2} \tag{A.21}$$

$$= I_0 \exp[(i\omega_0 - \lambda_0)t_0 + i\phi_0][A(\omega) + iD(\omega)] \tag{A.22}$$

in which the absorption, $A(\omega)$, and dispersion, $D(\omega)$, lineshapes can be expressed as

$$A(\omega) = \frac{\lambda_0}{\lambda_0^2 + (\omega_0 - \omega)^2} \tag{A.23}$$

$$D(\omega) = \frac{(\omega_0 - \omega)}{\lambda_0^2 + (\omega_0 - \omega)^2} \tag{A.24}$$

The linewidth of the absorptive Lorentzian is defined as the full-width at half-height (FWHH) and is given by $\Delta\omega_{FWHM} = 2\lambda_0$ or $\Delta\nu_{FWHM} = \lambda_0/\pi$.

The maximum and minimum cusps of the dispersive lineshape are separated by exactly the absorptive linewidth. Note that for large frequency offsets, the decay of the absorptive Lorentzian lineshape is proportional to $1/(\omega_0 - \omega)^2$, but the decay of the dispersive Lorentzian lineshape is proportional to $1/(\omega_0 - \omega)$. Accordingly, absorptive-phase lineshapes yield much more highly resolved NMR spectra and are greatly preferred to dispersive lineshapes.

Because the free induction decay is sampled digitally, the experi- mental frequency domain spectrum is calculated using the discrete Fourier transform

$$S(\nu) = S(k/N\Delta t) = F\{s(j\Delta t)\} = \sum_{j=0}^{N-1} s(j\Delta t)e^{-i2\pi jk/N} \tag{A.25}$$

in which N is the number of (complex) data points, Δt is the sampling interval, $k = -N/2, \cdots, 0, \cdots, N/2$, and the digitized signal, corresponding to the continuous signal, is described by

$$s(j\Delta t) = I_0 \exp[(i\omega_0 - \lambda_0)(j\Delta t + t_0) + i\psi_0] \tag{A.26}$$

The inverse transform is given by

$$s(j\Delta t) = F^{-1}\{S(k/N\Delta t)\} = \frac{1}{N}\sum_{t=0}^{N-1} S(k/N\Delta t)e^{i2\pi jk/N} \tag{A.27}$$

The frequency range represented by the Fourier transformed signal is $-1/(2\Delta t) \leq \nu \leq 1(2\Delta t)$ in discrete steps of $\Delta\nu = 1/(N\Delta t)$. In terms of the Nyquist frequency, $f_n \leq \nu \leq f_n$ the discrete Fourier transform of the N input signal points yields N+1 frequency domain data points. In fact, $S(f_n) = S(-f_n)$, so that only N unique points are obtained in the frequency-domains function. Most Fourier transformation algorithms provide as output the N points for $k = -N/2, \cdots, N/2 - 1$; i.e., the point $S(f_n)$ is not returned. Consequently, the zero frequency point in the frequency domain spectrum is not $k = N/2$ but rather $k = N/2 + 1$. The discrete Fourier transform can be expressed as

$$S(\omega_k) = I_o \exp[(i\omega_0 - \lambda_0)t_0 + i\psi_0]\frac{1 - \exp[N\Delta t(i\omega_0 - i\omega_k - \lambda_0)]}{1 - \exp[\Delta t(i\omega_0 - i\omega_k - \lambda_0)]} \tag{A.28}$$

in which $\omega_k = 2\pi k/(N\Delta t)$ and the series has been summed using the identity

$$\sum_{j=0}^{N-1} x^j = \frac{1-x^N}{1-x} \tag{A.29}$$

discrete Fourier transform can be represented in the $I_0 \exp[(i\omega_0 - \lambda_0)t_0 + i\phi_0][A(\omega) + iD(\omega)]$ form if $\Delta t \to 0$ and $N \to \infty$ while $N\Delta t\lambda_0 \gg 1$. This limit represents quasi-continuous sampling of the time-domain signal until it has completely decayed.[62]

Appendix B

Fast Fourier transform

In 1965 a method of computing discrete Fourier transforms suddenly became widely known(Cooley and Tukey, 1965) and revolutionized many fields where onerous computing was an impediment to progress.

There are various ways of understanding thsi fast fourier transform(FFT). One way, which will appeal to certain people, is in terms of factorization of the transform matrix. From the definition, we can write the DFT relation(for N=8) in the form of a matrix product,

$$\begin{bmatrix} F(0) \\ F(1) \\ F(2) \\ F(3) \\ F(4) \\ F(5) \\ F(6) \\ F(7) \end{bmatrix} = \begin{bmatrix} 1 & 1 & 1 & 1 & 1 & 1 & 1 & 1 \\ 1 & \omega & \omega^2 & \omega^3 & \omega^4 & \omega^5 & \omega^6 & \omega^7 \\ 1 & \omega^2 & \omega^4 & \omega^6 & \omega^8 & \omega^{10} & \omega^{12} & \omega^{14} \\ 1 & \omega^3 & \omega^6 & \omega^9 & \omega^{12} & \omega^{15} & \omega^{18} & \omega^{21} \\ 1 & \omega^4 & \omega^8 & \omega^{12} & \omega^{16} & \omega^{20} & \omega^{24} & \omega^{28} \\ 1 & \omega^5 & \omega^{10} & \omega^{15} & \omega^{20} & \omega^{25} & \omega^{30} & \omega^{35} \\ 1 & \omega^6 & \omega^{12} & \omega^{18} & \omega^{24} & \omega^{30} & \omega^{36} & \omega^{42} \\ 1 & \omega^7 & \omega^{14} & \omega^{21} & \omega^{28} & \omega^{35} & \omega^{42} & \omega^{49} \end{bmatrix} \times \begin{bmatrix} f(0) \\ f(1) \\ f(2) \\ f(3) \\ f(4) \\ f(5) \\ f(6) \\ f(7) \end{bmatrix}$$

where $\omega = \exp(-i2\pi/N)$. The quantity ω is an Nth root of unity, since $\omega^N =$

$\exp(-i2\pi) = 1$. It may be thought of a complex number whose modulus is unity and whose phase is -(1/N) turns.

$$\begin{bmatrix} F(0) \\ F(1) \\ F(2) \\ F(3) \\ F(4) \\ F(5) \\ F(6) \\ F(7) \end{bmatrix} = \begin{bmatrix} 1 & 0 & 0 & 0 & 1 & 0 & 0 & 0 \\ 0 & 1 & 0 & 0 & 0 & \omega & 0 & 0 \\ 0 & 0 & 1 & 0 & 0 & 0 & \omega^2 & 0 \\ 0 & 0 & 0 & 1 & 0 & 0 & 0 & \omega^3 \\ 1 & 0 & 0 & 0 & \omega^4 & 0 & 0 & 0 \\ 0 & 1 & 0 & 0 & 0 & \omega^5 & 0 & 0 \\ 0 & 0 & 1 & 0 & 0 & 0 & \omega^6 & 0 \\ 0 & 0 & 0 & 1 & 0 & 0 & 0 & \omega^7 \end{bmatrix} \times \begin{bmatrix} 1 & 0 & 1 & 0 & 0 & 0 & 0 & 0 \\ 0 & 1 & 0 & \omega^2 & 0 & 0 & 0 & 0 \\ 1 & 0 & \omega^4 & 0 & 0 & 0 & 0 & 0 \\ 0 & 1 & 0 & \omega^6 & 0 & 0 & 0 & 0 \\ 0 & 0 & 0 & 0 & 1 & 0 & 1 & 0 \\ 0 & 0 & 0 & 0 & 0 & 1 & 0 & \omega^2 \\ 0 & 0 & 0 & 0 & 1 & 0 & \omega^4 & 0 \\ 0 & 0 & 0 & 0 & 0 & 1 & 0 & \omega^6 \end{bmatrix} \times$$

$$\begin{bmatrix} 1 & 1 & 0 & 0 & 0 & 0 & 0 & 0 \\ 1 & \omega^4 & 0 & 0 & 0 & 0 & 0 & 0 \\ 0 & 0 & 1 & 1 & 0 & 0 & 0 & 0 \\ 0 & 0 & 1 & \omega^4 & 0 & 0 & 0 & 0 \\ 0 & 0 & 0 & 0 & 1 & 1 & 0 & 0 \\ 0 & 0 & 0 & 0 & 1 & \omega^4 & 0 & 0 \\ 0 & 0 & 0 & 0 & 0 & 0 & 1 & 1 \\ 0 & 0 & 0 & 0 & 0 & 0 & 1 & \omega^4 \end{bmatrix} \times \begin{bmatrix} 1 & 0 & 0 & 0 & 0 & 0 & 0 & 0 \\ 0 & 0 & 0 & 0 & 1 & 0 & 0 & 0 \\ 0 & 0 & 1 & 0 & 0 & 0 & 0 & 0 \\ 0 & 0 & 0 & 0 & 0 & 0 & 1 & 0 \\ 0 & 1 & 0 & 0 & 0 & 0 & 0 & 0 \\ 0 & 0 & 0 & 0 & 0 & 1 & 0 & 0 \\ 0 & 0 & 0 & 1 & 0 & 0 & 0 & 0 \\ 0 & 0 & 0 & 0 & 0 & 0 & 0 & 1 \end{bmatrix} \times \begin{bmatrix} f(0) \\ f(1) \\ f(2) \\ f(3) \\ f(4) \\ f(5) \\ f(6) \\ f(7) \end{bmatrix}$$

This factorization leaves only two nonzero elements in each row. In first matrix there are N^2 multiplications but there are only 2N multiplication per factor if we use second matrix equation, and the number of factors M is given by $2^M = N$ if we do not count the first factor, which merely represents a rearrangement. Thus the multiplications total $2N \log_2 N$. Examination of the factors shows that many of the multiplications are trivial, and therefore to calculate the precise time saving will require careful attention to details. Nevertheless, we are better off by a factor of N which arise with a long data trains or with digitized two dimensional images such as photograph, for example.[63]

Here is another method of understanding the fast Fourier transform. A sequence of N elements may be devided into two shorter sequences of N/2 elements each by placing

the even-numbered elements into first sequence and the odd-numbered ones into the second. For example,{8 7 6 5 4 3 2 1} can be split into {8 6 4 2 } and {7 5 3 1}. Each of these possesses a DFT. From these two DFT's how could one obtain the DFT of the longer sequence? The answer is obtained by writing

$$\{87654321\} = \{80604020\} + \{07050301\} \tag{B.1}$$

We see that the described DFT can be obtained by using the streching and shift theorem. From the streching theorem we know that if

$$\{8642\} \supset \{ABCD\} \tag{B.2}$$

then

$$\{80604020\} \subset \frac{1}{2}\{ABCDABCD\} \tag{B.3}$$

a phenomenon that may be familiar from Fourier series coefficients for periodoc functions.
Likewise, if

$$\{7531\} \supset \{PQRS\} \tag{B.4}$$

then

$$\{70503010\} \subset \frac{1}{2}\{PQRSPQRS\} \tag{B.5}$$

Now we apply the shift theorem to find that

$$\{70503010\} \subset \frac{1}{2}\{P \;\; \omega Q \;\; \omega^2 R \;\; \omega^3 S \omega^4 P \;\; \omega^5 Q \;\; \omega^6 R \;\; \omega^7 S\} \tag{B.6}$$

Multiplication by ω means rotation by one Nth of revolution in the complex plane, so the effect of the shift is to apply a phase delay that increase progressively along the sequence of elements {P Q R S P Q R S}. Adding 1.39 and 1.42 gives the DFT

of the long sequence. Thus the transformation with N=8 has been broken down into two transformations with N=4, which potentially represents a 50 percent time saving, since the number of multiplications in a DFT performed according to (1) goes as N^2. To see how this breaking down can be taken even further. Starting with the given sequence on the left, we rearrange it into the two short sequences {8 6 4 2} and {7 5 3 1} that form the inputs to two transformers with N=4 whose outputs are {A B C D} and {P Q R S}, respectively. The unbroaken flow lines show that A, B, C, and D are transferred to the output nodes to deliver {A B C D A B C D}. The broken flow lines are tagged with factors that cause the delivery of P, ωQ, ω^2R, etc., as in equation 1.42 to the same output nodes, where addition takes place.[63]

Finally, the steps may be summarized as follows. First, we rearrange th given sequence into {8 7 6 5 4 3 2 1}, an operation corresponding exactly to multiplication by the first square matrix of (2) and sometimes loosly referred to as bit reversal. Then eight new numbers are calculated as linear combinations of various pairs of rearranged data, exactly as indicated by second square matrix of (2). There are two more similar stages, making a total of three such operations in all(or M, in general, where $2^M = N$). Of course, not all the 48 multiplications are significant. There are 32 multiplications by unity and 7 multiplications by ω^4, which is simply a sign reversal. In addition, ω^2 and ω^6 are rather simple to handle.

Appendix C

Data Processing

It is very rare that a spectrum obtained by Fourier transformation of a free induction decay satisfies all demands with regard to optimum presentation. In most cases, it is desirable to subject the data to a linear filtering procedure to optimize the appearance of the spectrum. The restriction to linear processes is justified since it allows the processing of overlapping resonance lines without causing inteference effects.
Linear transformation processes can always be represented by a convolution integral of the signal and the impulse responce of the filter process. In the context of Fourier spectroscopy, the spectrum S(ω) must be submitted to a filtering process characterized by a frequency-domain filter function H(ω)

$$S_f(\omega) = H(\omega) \star S(\omega) \tag{C.1}$$

The convolution integral can be evaluated directly, but one may take advantage of the convolution theorem and multiply the time-domain signal s(t) with the corresponding time-domain filter function h(t)

$$s_f(t) = h(t).s(t) \tag{C.2}$$

where h(t) is the Fourier transform of H(ω).
We may identity H(ω) with the 'impulse response', while h(t) now represents the 'frequency response' of the filter. To avoid semantic difficulties in the distinction of the two function, we prefer to use the more neutral terms 'frequency-domain' and 'time-domain filter function' for H(ω) and h(t), respectively.

Equation 1.44 demonstrates that filtering in Fourier spectroscopy boils down to the multiplication of the free induction signal with a suitable weighing function h(t) prior to Fourier transformation. It is one of the virtues of Fourier spectroscopy that filtering can be achieved in this extremely simple and convenient manner, perhaps with the only disadvantage that a Fourier transformation must be computed before the effect of a filter function on the spectrum can be appreciated.[62]

The purposes of filtering may be quite diverse, and we shall mention only few of the many possible application.

1. Matched filtering to maximize the sensitivity(signal-to-noise ratio) in one- and in two-dimensional spectroscopy.
2. Resolution enhancement by artificially narrowing the resonance lines.
3. Lineshapes transformation
4. Apodization of free induction decays to suppress oscillating signal tails ('ripple') in the spectrum.
5. Pseudo-echo filtering to eliminate dispersive contributions to line-shapes in two-dimentional spectroscopy.
6. Correction of instrumental distortions, caused for example by a finite response time.

In the following, we shall briefly discuss apolization and resolution enhancement, as they are not adequately covered in the later parts of this volume. A few remarks

on resolution enhancement by zero-filling and linear prediction methods will conclude this section.

C.1 Apodization

In practical Fourier spectroscopy, the acquisition time t_{max} of the free induction decay is always limited and the signal s(t) is known only for $0 \leq t \leq t_{max}$. This may severely limit the resolution of the spectrum, since one is restricted to calculating the Fourier transform of a truncated signal

$s_{trunc}(t) = s(t)$ for $t \leq t_{max}$

$s_{trunc}(t) = 0$ for $t > t_{max}$

The truncated signal $s_{trunc}(t)$ can be thought of as the product of the untruncated signal s(t) with a rectangular weighing function,

$$s_{truc}(t) = s(t).\Pi(\frac{t}{2t_{max}}) \tag{C.3}$$

with

$\Pi(x) = 1$ for $-\frac{1}{2} < x < \frac{1}{2}$,

$\Pi(x) = 0$ for $|x| > \frac{1}{2}$

The corresponding Fourier spectrum is therefore obtained by convolution of the undistorted spectrum S(f) with the Fourier transform of the rectangular weighing function

$S_{trunc}(f) = S(f) \star 2t_{max} sinc(2t_{max} f)$

The sinc(x) function, defined by

$sinc(x) = \frac{\sin \pi x}{\pi x}$

produces oscillatory signal tails('ripple'), which may be highly undesirable as it severely limits resolution.

The oscillations arise from the sharp cut-off of the free induction signal which introduces high frequencies. It is the purpose of *apodization* to modify the envelope of the trucated signal by multiplication with a weighing function such that these oscillations are largely suppressed. It is obvious that the envelope must tend smoothy to zero at $t = t_{max}$ to prevent such oscillations. At the same time, care should be taken to avoid excessive line-broadening.[62]

The selection of a suitable weighing function h(t) to apodize truncated signals has been discussed in numerous papers in various fields of science, such as electrical communication, astronomy, and infra-red Fourier spectroscopy as well as in NMR. The approaches range from inspired guesswork to computer optimization and purely theoretical derivations.

In the context of digital signal processing by Fourier transformation, apodization is often called "windowing". This term suggests that truncation errors can be minimized by properly shaping the window through which the data is observed. A certain broadening has to be admitted to minimize the amplitude of the ripple, and the larger the acceptable broadening the better the suppression of the ripple. The theoretical optimum is reached by so-called Dolph-Chebycheff window. This class of windows minimizes the relative ripple amplitude for any predetermined broadening B of the resonance lines.[62]

Unfortunately there is no analytical expression for the optimum weighting function h(t), but it can be obtained numerically by Fourier-transforming the corresponding frequency domain filter function H(f)

$$H(f) = \frac{\cos\{2P\cos^{-1}[z_0\cos(\pi f/v_0)]\}}{\cosh\{2P\cosh^{-1}(z_0)\}} \tag{C.4}$$

where P+1 is the number of sampling points of the free induction decay, ν_s is the sampling rate, and the quantity

$$z_0 = [\cos(\pi B/2\nu_s)]^{-1} \approx 1 + \pi^2 B^2/(8\nu_s^2) \tag{C.5}$$

is determined by the allowed broadening B(expressed in Hz). H(f) corresponds then to the lineshapes obtained for a line of infinitely narrow natural width.

In most practical applications it is not necessary to afford the trouble of adjusting the apodization function to the number of sampling points. Numerous simple approximations are known, particularly in the field of digital data-processing.

C.2 Resolution Enhancement

While apodization aims at a faithful representation of the spectrum, resolution enhancement attempts to achieve a transformation of the lineshape to narrow the resonance lines artificially.

In principle, it is possible to select an arbitrary desired lineshape $S_f(\omega)$ and to compute a weighing function h(t) which will transform the experiemental into the desired lineshape. The transformation can be obtained by multiplying th free induction decay with the function

$$h(t) = s_f^e(t)/s^e(t) \tag{C.6}$$

where $s^e(t)$ is the envelope of the recorded free induction signal, and $s_f^e(t)$ is the desired envelope, i.e. $s_f^e(t) = F^{-1}\{S_f(\omega)\}$. In other words, the signal s(t) is stripped of its 'natural' envelope $s^e(t)$ and is fitted out with an envelope s_f^e that produces the desired lineshape after Fourier transformation.[62]

In practice, however, two restrictions have to be taken into account

1. Resolution enhancement necessarily implies the enhancement of the later parts of the free induction signal, since the weighing function h(t) increase with t. Random noise contributions in the later parts of the signal may therefore be excessively enhanced, and the sensitivity may be deteriorated beyond an acceptable limit. A useful resolution enhancement function h(t) should therefore

always decay towards zero for large t, in order to abtain a compromise between resolution and sensitivity.

2. The achievable resolution enhancement is often restricted by the fact that the local acquisition time t_{max} is limited, and an appreciable resolution enhancement is only feasible when the sampling period is extended.

We limit the discussion to some widely used resolution enhancement function:

1. *Lorentz-Gauss transformation*: Assuming that the natural decay is exponential with a time constant $T_2^\star$, multiplication of the free induction signal with the weighing function

$$h(t) = \exp\{t/T_2^\star - \sigma^2 t^2/2\} \tag{C.7}$$

strips the line of its Lorentzian character with half-width at half-height $\omega_{\frac{1}{2}} = 1/T_2^\star$ and fits it out with a Gaussian shape

$$S(\omega) = \frac{\sqrt{2\pi}}{\sigma} \exp\{\frac{-\omega^2}{2\sigma^2}\} \tag{C.8}$$

with a half-width at half-height $\omega_{\frac{1}{2}} = 1.177\sigma$. By adjusting the parameter σ, it is in principle possible to achieve an arbitrary degree of line-narrowing, disregarding for the moment the limitations imposed by the finite acquisition time t_{max}. The Gaussian shape has the advantage that the resonance lines have 'tails' that are less pronounced. At the same time, a fair apodization of the FID is achieved, thus reducing problems with truncation.

2. *Sine-bell function*: Multiplication of the free induction signal with a sine-bell function with a period equal to twice the aquisition time t_{max}

$$h(t) = \sin(\pi t/t_{max}) \tag{C.9}$$

has the desired effect of giving the free induction signal an envelope that increases with time and that is apodized towards zero for t approaching t_{max}.

The application of this function is extremely simple, since it has no adjustable parameter, but the resolution enhancement is limited. The resulting lineshape vanishes, which implies the presence of negative signal tails that distort the baseline of the spectrum. The deficiency can be slightly improved by shifting the phase of the sine-bell.[62]

C.3 Linewidth

The phenomenological linewidth is defined as the full-width at half-height of the resonance lineshape and is a primary factor affecting both resolution and signal-to-noise ratio of NMR spectra. For a lorentzian lineshape, the homogeneous linewidth is given by $\Delta\nu_{FWHM} = R_2/\pi$ in hertz(or $\Delta\omega_{FWHM} = 2R_2$ in rad/s) and the inhomogeneous linewidth is $\Delta\nu_{FWHM} = R_2^*/\pi$, in which $R_2^*/\pi = R_2 + R_{inhom}$ and R_{inhom} represents the broadening of the resonance signal due to inhomogeneity of magnetic field. In modern NMR spectrometers R_{inhom}/π is on the order of 1Hz. Values of R_2(and hence homogeneous linewidths) are approximately prportional to the overall rotational correlation time of th eprotein and thus depend on molecular mass and shape of the molecule. Observed linewidths significantly larger than expected based on the molecular mass of the protein imply that aggregation is increasing the apparent rotational correlation time or that chemical exchange effects contribute significantly to the inhomogeneous linewidth.[62]

Given theoretical or experimental estimates of τ_c, the theoretical equation can be used to calculate approximate values of resonance linewidths. The principal uncertainties in the calculation are due to following factors:

1. Anisotropic rotational diffusion of nonspherical molecules.

2. Differential contribution from internal motion(particularly in loops or for side chains).

3. Cross-correlation effects.

4. 1H dipolar interaction with all nearby protons(which depend on detailed structures of the proteins).

5. Incomplete knowledge of fundamental parameters[such as chemical shift anisotropies(CSA)].

In light of these uncertainties, the result should be regarded as approximate guidelines.

The correlation time for brownian rotational diffusion can be measured experimentally using time resolved fluoroscence spectroscopy, light scattering, and NMR spin relaxation spectroscopy, or calculated using a variety of hydrodynamic theories(that unfortunately require detailed information on the shape of the molecule). In the absence of more accurate information, th esimplest theoretical approach for approximately spherical globular proteins calculates th eisotropic rotational correlation time from the Stokes' law:

$$\tau_c = \frac{4\pi\eta_w r_H^3}{3k_B T} \tag{C.10}$$

in which η_w is the viscosity of the solvent, r_H is the effective hydrodynamic radius of the protein, k_B is Boltzmann's constant, and T is the temperature.[62]

Appendix D

Stejskal and Tanner Equation

Bloch Equations Including the Effects of Diffusion [5]. The Bloch equations for the macroscopic nuclear magnetization $M(r,t) = M_x + M_y + M_z$, including the diffusion of magnetization, are given by

$$\frac{\partial M(r,t)}{\partial t} = \gamma M \times B(r,t) - \frac{M_x i + M_y j}{T_2} - \frac{(M_z - M_0)k}{T_1} + D\nabla^2 M \tag{D.1}$$

In he case of anisotropic diffusion, the last term in the equation would be replaced by $\nabla.D.\nabla M$. If we take B_0 to be oriented along z axis and that this is superposed by gradient g vanishing at the origin which is parallel to B_0, and thus we can write $B_x = 0, B_y = 0$,

$$B_z = B_0 + (g.r) = B_0 + g_x x + g_x y + g_z z \tag{D.2}$$

If equation 2.7 is then substituted into equation 2.6, noting that

$$M \times B = (M_y B_z - M_z B_y)_x + (M_z B_x - M_x B_z)_y + (M_x B_y - M_y B_x)_z \tag{D.3}$$

and defining the transverse magnetization as $m = M_x + iM_y$ we obtain

$$\frac{\partial m}{\partial t} = -i\omega_o m - i\gamma(g.r)m - \frac{m}{T_2} + D\nabla^2 m \tag{D.4}$$

The Stejskal and Tanner Pulse Sequence in the Absence of Diffusion[5]. In the absence of diffusion(i.e. $D = 0$), m relaxes exponentially with a time constant T_2, and thus we set

$$m = \psi e^{-i\omega_0 t - \frac{t}{T_2}} \tag{D.5}$$

where ψ represents the amplitude of the precessing magnetization unaffected by the effects of relaxation. If we substitute equation 2.10 into equation 2.9, we obtain

$$\frac{\partial \psi}{\partial t} = -i\gamma(g.r)\psi + D\nabla^2\psi \tag{D.6}$$

In the absence of diffusion, equation 2.11 is a first-order ordinary differential equation with solution

$$\psi(r,t) = S\exp(-i\gamma r.F) \tag{D.7}$$

where S is a constant and

$$F(t) = \int_0^t g(t')dt' \tag{D.8}$$

Now, if we consider the case of the PFG pulse sequence, then during the period from the $\pi/2$ pulse to the π pulse, we have now

$$\psi(r,t) = S\exp(-i\gamma r.F) \tag{D.9}$$

and S corresponds to the value of ψ immediately after the $\pi/2$ pulse. After the π pulse, we have

$$\psi(r,t) = S\exp(-i\gamma r.(F - 2f)) \tag{D.10}$$

where $f = F(\tau)$. Thus we can see that the effect of the π pulse is to set back the phase of ψ by twice the amount that it had advanced up until the π pulse. Then

equation 2.15 can be combined into

$$\psi(r,t) = S\exp(-i\gamma r.(F - 2H(t-\tau)f)) \tag{D.11}$$

where H(t) is the Heaviside step function. We not here that above equation is valid for the Hahn spin-echo pulse sequence.

The Stejskal and Tanner Pulse Sequence in the Presence of Diffusion[5]. In the above paragraph we considered the solution to previous in the absence of the diffusion. In this section, we derive a solution to Eq. w41x including the effects of diffusion. We assume a solution to above equation, including the diffusion term, to be of the form of above equation but allow S to be a function of t [i.e., S(t)]. Now we obtain

$$\frac{dS(t)}{dt} = -\gamma^2 D[F - 2H(t-\tau)f]^2 s(t) \tag{D.12}$$

Now we integrate above equation from $t = 0$ to $t = 2\tau$

$$\ln[\frac{S(2\tau)}{S(0)}] = \ln(E(2\tau)) \tag{D.13}$$

$$= \int_0^{\tau} -\gamma^2 D F^2 dt + \int_{\tau}^{2\tau} -\gamma^2 D[F - 2f]^2 dt \tag{D.14}$$

$$= -\gamma^2 D\{\int_0^{2\tau} F^2 dt - 4f\int_{\tau}^{2\tau} F dt + 4f^2\tau\} \tag{D.15}$$

The application of equation 2.20 to the calculation of the echo attenuation resulting from the effects of diffusion and the application of gradients is quite straightforward but rather tedious. If we apply the gradient pulses as shown in the spin echo pulse sequences and neglect the effects of any background gradients, then we can define g(t) and the effective field gradient, $g_{eff}(t)$. Using definition 2.13 of g(t), F(t) for $t_1 + \Delta < t`t_1 + \Delta + \delta$ is calculates as follows,

$$F(t) = \int_0^{t_1} 0dt + \int_{t_1}^{t_1+\delta} g dt + \int_{t_1+\delta}^{t_1+\Delta} 0dt + \int_{t_1+\Delta}^{t} g dt \tag{D.16}$$

$$= g(t + \delta - t_1 - \Delta) \tag{D.17}$$

We obtain the result

$$\ln(E) = -\gamma^2 g^2 D\delta^2(\Delta - \delta/3) \tag{D.18}$$

The term $\delta/3$ accounts for the finite width of the gradient pulse. Equation 2.23 is not a function of t_1, and thus the placement of the gradient pulses in the sequence is of no consequence; for example, there is no requirement that the gradient pulses be symmetrically placed around the π pulse. If instead we had imposed a steady gradient throughout the echo sequence(i.e. $\Delta = \delta = \tau$), we would have reproduced the well-known diffusion term in the expression for the intensity of the Hahn spin-echo sequence, as expected.[5]

Appendix E

Spin Echo Pulse Sequence

E.0.1 Pulse sequence

Pulsed field gradient NMR (PFGNMR) method consists of two-rf-pulse Hahn-echo experiment with identical magnetic field gradient pulses of magnitude g, duration δ and separation Δ applied respectively during the dephasing and rephasing segments of the echo cycle (Figure E.1. The first gradient produces a rapid precessional phase shift depending on the position of each nucleus in the sample. Between gradient pulses the molecules containing the nuclei change position due to diffusion. In the intervening period, the 180°rf pulse inverts all previous phase shifts so that the second gradient has the effect of producing phase compensation, thus forming an echo. To the extent that motion has occurred, the refocusing is incomplete and the consequent attenuation of the spin echo gives a measure of the ensemble average of nuclear translations. The two gradient thus record respectively the initial and subsequent positions of the nuclei over the well defined time scale Δ, and hence PFGNMR is well suited to examine the displacement time dependence.

The echo at 2τ has magnitude

$$S(2\tau) = M_o exp(-2\tau/T_2) exp[-Dq^2(\Delta - \delta/3)] \tag{E.1}$$

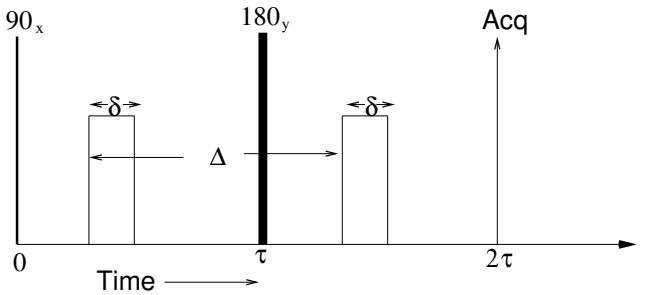

FIGURE E.1: The spin-echo (SE) pulse sequence

where M_o is the equilibrium magnetization and q=$\gamma g\delta$ is the area of the gradient pulse. The correction term $\delta/3$ is because of rectangular gradient shape. The maximum possible signal is recovered in the absence of relaxation effects and chemical shifts are refocused at the echo. T_2 can be short for slowly tumbling macromolecules but then this lead to a severe loss of signal. J-modulation refers to signal modulation resulting from hard RF pulses that exchange the spin states of nuclei that are coupled to the nuclei of interest thus preventing complete refocusing. These effects present special problems for strongly coupled spin systems [16].

Bibliography

[1] Steven L. Fiedler and Angela Violi. Simulation of nanoparticle permeation through a lipid membrane. *Biophysical Journal*, 99:144–152, July 2010.

[2] Geoffrey D Bothun. Hydrophobic silver nanoparticles trapped in lipid bilayer: Size distribution, bilayer phase behavior, and optical properties. *Journal of Nnaobiotechnology*, 6, November 2008.

[3] P. Gkeka J.P. Prates Ramalho and L. Sarkisov. Structure and phase transformations of dppc lipid bilayers in the presence of nanoparticles: Insights from coarse-grained molecular dynamics simulations. *Langmuir*, 27:3723–3730, March 2011.

[4] Harald Gunther. *NMR Spectroscopy: Basic Principles, Concept, and application in Chemistry.* John Wiley & Sons, 1992.

[5] William S. Price. Pulsed-field gradient nuclear magnetic resonance as a tool for studying translational diffusion: Part 1. basic theory. *Concepts Magn Reson*, 9: 299–336, 1997.

[6] Hans-Eckhardt Schaefer. *Nanoscience: The Science of the small in Physics, Engineering, Chemistry, Biology and Medicine.* Springer, 2010.

[7] *Principles of Biochemistry.* Lehninger.

[8] Amrish Menjoge Monica Sanders, Robert Mueller and Sergey Vasenkov. Pulsed field gradient nuclear magnetic resonance study of time-dependent diffusion behavior and exchange of lipids in plannar-supported lipid bilayers. *J. Phys. Chem. B*, 113:14355–14364, September 2009.

[9] C.B. Powar. *Cell Biology*. Himalaya Publishing House, 2008.

[10] Monica Olvera de la Cruz Doris Grillo and Igal Szleifer. Theoretical studies of the phase behavior of dppc bilayers in the presence of macroions. *Soft Matter*, 2011.

[11] Tiina Roose Maurits R.R. de Planque, Sara Aghdaei and Hywel Morgan. Electrophysiological characterization of membrane disruption by nanoparticles. *ACS NANO*, 5(5):3599–3606, April 2011.

[12] Zhen Chen Jiaqi Lin, Hongwu Zhang and Yonggang zheng. Penetration of lipid membranes by gold nanoparticles: Insight into cellular uptake, cytotoxicity, and their relationship. *ACS NANO*, 4(9):5421–5429, August 2010.

[13] D. S. Webster and K. H. Marsden. Improved apparatus for the nmr measurement of self [U+2010] diffusion coefficients using pulsed field gradients. *Rev. Sci. Instrum.*, 1974.

[14] Moseley M. Lindman, B. and P. Stilbs. Fourier transform nmr self-diffusion and microemulsion structure. *J Colloid Interface Sci*, 1981.

[15] J. S. Murday and R. M. Cotts. Self [U+2010] diffusion in liquids: H2o, d2o, and na. *J. Chem. Phys.*, 1970.

[16] R. Vold and R. Vold. *Prog. Nuc. Magn. Reson.*, 1978.

[17] K.F. Morris and C.S. Johnson Jr. *J. Am. Chem. Soc.*, 1993.

[18] J. Van Duynhoven R. Huo, R. Wehrens and L.M.C. Buydens. Assessment of techniques for dosy nmr data processing. *Analytica Chimica Acta*, 2003.

[19] Vladimir P Torchilin, editor. *Nanoparticles as Drug Carriers*. Imperial College Press, 2006.

[20] Peter Rodgers, editor. *NANOSCIENCE AND TECHNOLOGY*. nature publisher group, 2010.

[21] Christopher A. Graowski Rami A. Omari, Andrew M. aneese and Ashis Mukhopadhyay. Diffusion of nanoparticles in semidilute and entangled polymer solutions. *The Journal of Physical Chemistry B Letters*, 113:8449–8452, May 2009.

[22] Anthony M. mrse Gabriele Canzi and Clifford P. Kubiak. Diffusion-ordered nmr spectroscopy as a reliable alternative to tem for determining the size of gold nanoparticles in organic solutions. *The Journal of Physical Chemistry C*, 115: 7972–7978, April 2011.

[23] M. Bergamin L. Feruglio F. Dinon A. Bianco E. Murano R. Marega, V. Aroulmoji and M. Prato. Two-dimensional diffusion-ordered nmr spectroscopy as a tool for monitoring functionalized carbon nanotube purification and composition. *ACS Nano*, 2010.

[24] Ribot F Escax V Verbruggen I Sanchez C Martins JC Biesemans M Van Lokeren L, Maheut G and Willem R. Characterization of titanium dioxide nanoparticles dispersed in organic ligand solutions by using a diffusion-ordered spectroscopy-based strategy. *Chem.-Eur. J.*, 2007.

[25] M Findeisen G.S Kapur and S Berger. Analysis of hydrocarbon mixtures by diffusion-ordered nmr spectroscopy. *Fuel*, 2000.

[26] M. A. Delsuc and T. E. Malliavin. Maximum entropy processing of dosy nmr spectra. *Anal. Chem.*, 1998.

[27] M-E Aubin-Tam and K Hamad-Schifferli. Structure and function of nanoparticle-protein conjugates. *Biomedical Material*, 3, 2008.

[28] Xi Li Bin Zhang Wei Li Hongyu Zhou, Fenfang Du and BING Yan. Characterization of organic molecules attached to gold nanoparticle surface using high resolution magic angle spinning ^1h nmr. *J. Phys. Chem C.*, 112:19360–19366, November 2008.

[29] V. Sue Myers Richard M. Crooks M. Victoria Gomez, Javier Guerra and Aldrik H. Velders. Nanoparticle size determination by ^1h nmr spectroscopy. *JACS Communications*, 131:14634–14635, September 2009.

[30] Ji-Young Mun Sung-hee Park, Seong-Geun Oh and Sung-Sik Han. Effects of silver nanoparticles on the fluidity of bilayer in phospholipid liposome. *Colloids and Surface B*, 44:117–122, June 2005.

[31] Y. H. Hu-Y. Hu H. S. Han N. Watson S. L. Chen-D. J. Irvine A. Verma, O. Uzun and F. Stellacci. Surface-structure-regulated cell-memmbrane penetration by monoleyer-protected nanoparticles. *Nat. Mater.*, 2008.

[32] S. C. Bae B. Wang, L. F. Zhang and S. Granick. Nanoparticle-induced surface raconstruction of phospholipid membranes. *Proc. Natl. Acad. Sci. U.S.A.*, 2008.

[33] A. R. Rammohan J. Balakrishnan D. R. Heine Y. Roiter, M. Ornatska and S. Minko. Interaction of nanoparticles with lipid membrane. *Nano Lett.*, 2008.

[34] R. Lipowsky and H. G. Dobereiner. Vescicles in contact with nanoparticles and colloids. *Europhys. Lett.*, 1998.

[35] M. Deserno and W. M. Gelbert. Adhesion and wrapping in colloid-vescicle complexes. *J. Phys. chem. B*, 2002.

[36] M. Deserno. When do fluid membranes engulf sticky colloids? *J. Phys.: Condens. Matter*, 2004.

[37] L. Livadaru and A. Kovalenko. Fundamental mechanism of translocation across liquidlike membranes: Toward control over nanoparticle behavior. *Nano Lett.*, 2006.

[38] V. V. Ginzburg and S. Balijepalli. Modeling the thermodynamics of the interaction of nanoparticles with cell membranes. *Nano Lett.*, 2007.

[39] S. Pogodin and V. A. Baulin. coarse-grained models of phospholipid membranes within the single chain mean field theory. *Soft Matter*, 2010.

[40] S. Pogodin and V. A. Baulin. Can a carbon nanotube pierce through a phospholipid bilayer? *ACS Nano*, 2010.

[41] S. J. Marrink and A. E. Mark. Coarse grained simulation of phase transitions of lipid membranes. *Biophys. J.*, 2005.

[42] D. Deamer and A.D. Bangham. Large volume liposomes by an ether vaporization method. *Biochimica et Biophysica Acta (BBA)-Biomembranes*, 1976.

[43] Weidong Wang Megan D. Reeves, Adam K. Schawel and Phoebe Dea. Effects of butanol isomers on dipalmitoylphosphatidylcholine bilayer membrane. *Biophysical Chemistry*, 2007.

[44] Ludwig Nissler Rolf Gebhardt Holger A. Scheidt, Andre Pampel and Daniel Huster. Investigation of the membrane localization and distribution of flavonoids by high-resolution magic angle spinning nmr spectroscopy. *Biochimica et Biophysica Acta*, 2004.

[45] D. S. Banks and C. Fradin. Anomalous diffusion of proteins due to molecular crowding. *Biophys. J.*, 2005.

[46] Fredrik Kartberg† Matthias Weiss, Markus Elsner† and Tommy Nilsson†. Anomalous subdiffusion is a measure for cytoplasmic crowding in living cells. *Biophysical Journal*, 2004.

[47] Joris Sprakel, Jasper van der Gucht, Martien A. Cohen Stuart, and Nicolaas A. M. Besseling. Rouse dynamics of colloids bound to polymer networks. *Phys. Rev. Lett.*, 99:208301, Nov 2007.

[48] Victor Pryamitsyn and Venkat Ganesan. Dynamics of probe diffusion in rod solutions. *Phys. Rev. Lett.*, 100:128302, Mar 2008.

[49] LJ Ye X.; Tong P.; Fetters. Colloidal sedimentation in polymer solutions. *Macromolecules*, 1998.

[50] Minerva Roman Clement N. Onyenemezu, Douglas Gold and Wilmer G. Miller. Diffusion of polystyrene latex spheres in linear polystyrene nonaqueous solutions. *Macromolecules*, 1993.

[51] Olle Soderman Harald Walderhaug and Daniell Topgaard. Self-diffusion in polymer systems studied by magnetic field-gradient spin-echo nmr methods. *Progress in Nuclear Magnetic Resonance Spectroscopy*, 2010.

[52] Tomasz Kalwarczyk Marcin Fialkowski Natalia Ziebacz, Stefan A. Wieczorek and Robert Holyst. Crossover regime for the diffusion of nanoparticles in polyethylene glycol solutions: influence of the depletion layer. *Soft Matter*, 7:7181, June 2011.

[53] Suliman Barhoum and Anand Yethiraj. An nmr study of macromolecular aggregation in a model polymer-surfactant solution. *The Journal Of Chemical Physics*, 132, January 2010.

[54] J.M. Harris and R.B. Chess. Effect of pegylation on pharmaceuticals. *Nat. Rev. Drug Discov.*, 2003.

[55] F. T. Greenaway J. J. Girerd G. Morgant J. C. Daran D. Nguyen-Huy B. Viossat, A. Tomas and J. R. J Sorenson. Low-temperature (180k) crystal structures of tetrakis-μ-(niflumato)di(aqua)dicopper(ii) n,n-dimethylformamide and n,n-dimethylacetamide solvates, their epr properties, and anticonvulsant activities of these and other ternary binuclear copper(ii)niflumate complexes. *J. Inorg Biochem.*, 2005.

[56] Warriner HE Zasadzinski JA Lu KW and Taeusch HW. Braun A, Stenger PC. A freeze-fracture transmission electron microscopy and small angle x-ray diffraction

study of the effects of albumin, serum, and polymers on clinical lung surfactant microstructure. *Biophys J.*, 2007.

[57] Decad GM and Nikaido H. Outer membrane of gram-negative bacteria. xii. molecular-sieving function of cell wall. *J Bacteriol.*, 1976.

[58] Vincent M. Stanford Kenneth A. Rubinson Oleg V. Krasilnikov Joseph W. F. Robertson, Claudio G. Rodrigues and John J. Kasianowicz. Single-molecule mass spectrometry in solution using a solitary nanopore. *Proc Natl Acad Sci U S A.*, 2007.

[59] Alexander D. MacKerell Jr. Hwankyu Lee, Richard M. Vanable and Richard W. Pastor. Molecular dynamics studies of polyethylene oxide and polyethylene glycol: Hydrodynamic radius and shape anisotropy. *Biophysical Journal*, 2008.

[60] Jorg Karger Konstantin Ulrich, Petrik Galvosas and Farida Grinberg. Effects of self-assembly on diffusion mechanism of triblock copolymer in aqueous solution. *Physical Review Letters*, 102, January 2009.

[61] William S. Price. Protein association studied by nmr diffusometry. *Current Opinion in colloid & Interface Science*, 11:19–23, November 2006.

[62] Geoffrey Bodenhausen Richard R. Ernst and Alexander Wokaun. *Principles of nuclear magnetic resonance in one and two dimensions.* CLARENDON PRESS-OXFORD, 1987.

[63] *The Fourier Transform and Its Applications.* Mcgraw Hill Higher Education, 2000.